RESE RCH RTICLE SUMM RY

OUTER SOLAR SYSTEM

Initial results from the New Horizons exploration of 2014 MU_{69} a small Kuiper Belt object

S A Stern *et al*

INTRODUCTION: The Kuiper Belt is a broad, torus-shaped region in the outer Solar System beyond Neptune s orbit. It contains primordial planetary building blocks and dwarf planets. NASA s New Horizons spacecraft conducted a flyby of Pluto and its system of moons on 14 July 2015. New Horizons then continued farther into the Kuiper Belt, adjusting its trajectory to fly close to the small Kuiper Belt object (486958) 2014 MU_{69} (henceforth MU_{69}; also informally known as Ultima Thule). Stellar occultation observations in 2017 showed that MU_{69} was ~25 to 35 km in diameter, and therefore smaller than the diameter of Pluto (2375 km) by a factor of ~100 and less massive than Pluto by a factor of ~10^6. MU_{69} is located about 1.6 billion kilometers farther from the Sun than Pluto was at the time of the New Horizons flyby. MU_{69} s orbit indicates that it is a "cold classical" Kuiper Belt object, thought to be the least dynamically evolved population in the Solar System. A major goal of flying past this target is to investigate accretion processes in the outer Solar System and how those processes led to the formation of the planets. Because no small Kuiper Belt object had previously been explored by spacecraft, we also sought to provide a close-up look at such a body s geology and composition, and to search for satellites, rings, and evidence of present or past atmosphere. We report initial scientific results and interpretations from that flyby.

RATIONALE: The New Horizons spacecraft completed its MU_{69} flyby on 1 January 2019, with a closest approach distance of 3538 km—less than one-third of its closest distance to Pluto. During the high-speed flyby, made at 14.4 km s ^{1}, the spacecraft collected ~50 gigabits of high-resolution imaging, compositional spectroscopy, temperature measurements, and other data on this Kuiper Belt object. We analyzed the initial returned flyby data from the seven scientific instruments carried on the spacecraft: the Ralph multicolor/panchromatic camera and mapping infrared composition spectrometer; the Long Range Reconnaissance Imager (LORRI) long–focal length panchromatic visible imager; the Alice extreme/far ultraviolet mapping spectrograph; the Radio Experiment (REX); the Solar Wind Around Pluto (SWAP) solar wind detector; the Pluto Energetic Particle Spectrometer Science Investigation (PEPSSI) high-energy charged particle spectrometer; and the Venetia Burney Student Dust Counter (VBSDC), a dust impact detector.

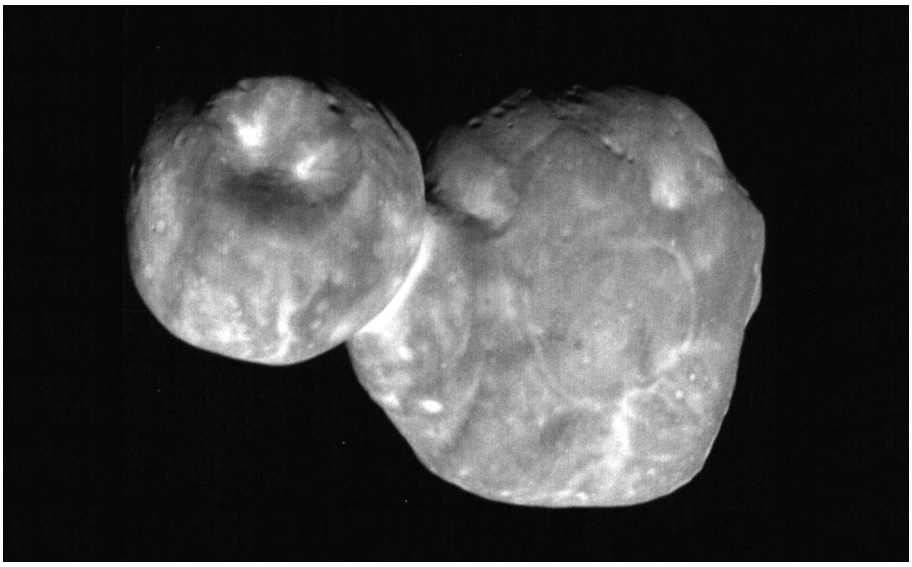

Image of MU_{69} from New Horizons LORRI observations taken 1 January 2019

RESULTS: Imaging of MU_{69} showed it to be a bilobed, contact binary. MU_{69} s two lobes appear to have formed close to one another, becoming an orbiting pair that subsequently underwent coupled tidal and orbital evolution to merge into the contact binary we observe today. The object rotates on its axis every 15.92 hours; its rotation pole is inclined approximately 98° to the plane of its heliocentric orbit. Its entire surface has a low visible-wavelength reflectivity (albedo) but displays brighter and darker regions across its surface, ranging from 5 to 12 reflectivity. The brightest observed regions are the "neck" of MU_{69}, where the two lobes are joined, and two discrete bright spots inside the largest crater-like feature on the object s surface. Although MU_{69} s albedo varies substantially across its surface, it is uniformly red in color, with only minor observed color variations. This coloration likely represents a refractory residue from ices and organic molecules processed by ultraviolet light and cosmic rays. Spectra of the surface revealed tentative absorption band detections due to water ice and methanol. The geology of MU_{69} consists of numerous distinct units but shows only a small number of craters, providing evidence that there is a deficit of Kuiper Belt objects smaller than ~1 km in diameter, and that there is a comparatively low collision rate in its Kuiper Belt environment compared to what would be expected in a collisional equilibrium population. A three-dimensional shape model derived from the images shows MU_{69} is not simply elongated but also flattened. The larger lobe was found to be lenticular, with dimensions of approximately 22 × 20 × 7 km (uncertainty <0.6 × 1 × 2 km), whereas the smaller lobe is less lenticular, with dimensions of approximately 14 × 14 × 10 km (uncertainty <0.4 × 0.7 × 3 km). No evidence of satellites, rings, or an extant atmosphere was found around MU_{69}.

CONCLUSION: Both MU_{69} s binarity and unusual shape may be common among similarly sized Kuiper Belt objects. The observation that its two lobes are discrete, have retained their basic shapes, and do not display prominent deformation or other geological features indicative of an energetic or disruptive collision indicates that MU_{69} is the product of a gentle merger of two independently formed bodies.

ON OUR WEBSITE

Read the full article at http://dx.doi.org/10.1126/science.aaw9771

All authors and affiliations are available in the full article online
*Corresponding author. Email: astern@boulder.swri.edu
Cite this article as S. A. Stern *et al*., *cience* **64**, eaaw9771 2019). DOI: 10.1126/science.aaw9771

RESE RCH RTICLE

OUTER SOLAR SYSTEM

Initial results from the New Horizons exploration of 2014 MU_{69} a small Kuiper Belt object

S. A. Stern[1]* H. A. Weaver[2] J. R. Spencer[1] C. B. Olkin[1] G. R. Gladstone[3] W. M. Grundy[4] J. M. Moore[5] D. P. Cruikshank[5] H. A. Elliott[3 6] W. B. McKinnon[7] J. Wm. Parker[1] A. J. Verbiscer[8] L. A. Young[1] D. A. Aguilar[9] J. M. Albers[2] T. Andert[10] J. P. Andrews[1] F. Bagenal[11] M. E. Banks[12] B. A. Bauer[2] J. A. Bauman[13] K. E. Bechtold[2] C. B. Beddingfield[5 14] N. Behrooz[2] K. B. Beisser[2] S. D. Benecchi[15] E. Bernardoni[11] R. A. Beyer[5 14] S. Bhaskaran[16] C. J. Bierson[17] R. P. Binzel[18] E. M. Birath[1] M. K. Bird[19 20] D. R. Boone[16] A. F. Bowman[2] V. J. Bray[21] D. T. Britt[22] L. E. Brown[2] M. R. Buckley[2] M. W. Buie[1] B. J. Buratti[16] L. M. Burke[2] S. S. Bushman[2] B. Carcich[2 23] A. L. Chaikin[24] C. L. Chavez[5 14] A. F. Cheng[2] E. J. Colwell[2] S. J. Conard[2] M. P. Conner[2] C. A. Conrad[1] J. C. Cook[25] S. B. Cooper[2] O. S. Custodio[2] C. M. Dalle Ore[5 14] C. C. Deboy[2] P. Dharmavaram[2] R. D. Dhingra[26] G. F. Dunn[3] A. M. Earle[18] A. F. Egan[1] J. Eisig[2] M. R. El-Maarry[27] C. Engelbrecht[2] B. L. Enke[1] C. J. Ercol[2] E. D. Fattig[3] C. L. Ferrell[1] T. J. Finley[1] J. Firer[2] J. Fischetti[13] W. M. Folkner[16] M. N. Fosbury[2] G. H. Fountain[2] J. M. Freeze[2] L. Gabasova[28] L. S. Glaze[29] J. L. Green[29] G. A. Griffith[2] Y. Guo[2] M. Hahn[20] D. W. Hals[2] D. P. Hamilton[30] S. A. Hamilton[2] J. J. Hanley[3] A. Harch[23] K. A. Harmon[16] H. M. Hart[2] J. Hayes[2] C. B. Hersman[2] M. E. Hill[2] T. A. Hill[2] J. D. Hofgartner[16] M. E. Holdridge[2] M. Horányi[11] A. Hosadurga[2] A. D. Howard[31] C. J. A. Howett[1] S. E. Jaskulek[2] D. E. Jennings[12] J. R. Jensen[2] M. R. Jones[2] H. K. Kang[2] D. J. Katz[2] D. E. Kaufmann[1] J. J. Kavelaars[32] J. T. Keane[33] G. P. Keleher[2] M. Kinczyk[34] M. C. Kochte[2] P. Kollmann[2] S. M. Krimigis[2] G. L. Kruizinga[16] D. Y. Kusnierkiewicz[2] M. S. Lahr[2] T. R. Lauer[35] G. B. Lawrence[2] J. E. Lee[36] E. J. Lessac-Chenen[13] I. R. Linscott[37] C. M. Lisse[2] A. W. Lunsford[12] D. M. Mages[16] V. A. Mallder[2] N. P. Martin[38] B. H. May[39] D. J. McComas[3 40] R. L. McNutt Jr.[2] D. S. Mehoke[2] T. S. Mehoke[2] D. S. Nelson[13] H. D. Nguyen[2] J. I. Núñez[2] A. C. Ocampo[29] W. M. Owen[16] G. K. Oxton[2] A. H. Parker[1] M. Pätzold[20] J. Y. Pelgrift[13] F. J. Pelletier[13] J. P. Pineau[41] M. R. Piquette[11] S. B. Porter[1] S. Protopapa[1] E. Quirico[28] J. A. Redfern[1] A. L. Regiec[2] H. J. Reitsema[42] D. C. Reuter[12] D. C. Richardson[30] J. E. Riedel[16] M. A. Ritterbush[16] S. J. Robbins[1] D. J. Rodgers[2] G. D. Rogers[2] D. M. Rose[1] P. E. Rosendall[2] K. D. Runyon[2] M. G. Ryschkewitsch[2] M. M. Saina[2] M. J. Salinas[13] P. M. Schenk[43] J. R. Scherrer[3] W. R. Schlei[2] B. Schmitt[28] D. J. Schultz[2] D. C. Schurr[29] F. Scipioni[5 14] R. L. Sepan[2] R. G. Shelton[2] M. R. Showalter[14] M. Simon[2] K. N. Singer[1] E. W. Stahlheber[2] D. R. Stanbridge[13] J. A. Stansberry[44] A. J. Steffl[1] D. F. Strobel[45] M. M. Stothoff[3] T. Stryk[46] J. R. Stuart[16] M. E. Summers[47] M. B. Tapley[3] A. Taylor[13] H. W. Taylor[2] R. M. Tedford[1] H. B. Throop[15] L. S. Turner[2] O. M. Umurhan[5 14] J. Van Eck[2] D. Velez[16] M. H. Versteeg[3] M. A. Vincent[1] R. W. Webbert[2] S. E. Weidner[40] G. E. Weigle II[48] J. R. Wendel[29] O. L. White[5 14] K. E. Whittenburg[2] B. G. Williams[13] K. E. Williams[13] S. P. Williams[2] H. L. Winters[2] A. M. Zangari[1] T. H. Zurbuchen[29]

The Kuiper Belt is a distant region of the outer Solar System. On 1 January 2019, the New Horizons spacecraft flew close to 486958) 2014 MU_{69}, a cold classical Kuiper Belt object approximately 30 kilometers in diameter. Such objects have never been substantially heated by the Sun and are therefore well preserved since their formation. We describe initial results from these encounter observations. MU_{69} is a bilobed contact binary with a flattened shape, discrete geological units, and noticeable albedo heterogeneity. However, there is little surface color or compositional heterogeneity. No evidence for satellites, rings or other dust structures, a gas coma, or solar wind interactions was detected. MU_{69} s origin appears consistent with pebble cloud collapse followed by a low-velocity merger of its two lobes.

he Kuiper Belt, a torus-shaped ensemble of objects in the outer Solar System beyond the orbit of Neptune, was discovered in 1992. This is the source region for Jupiter-family comets and contains primordial planetesimals and dwarf planets [e.g., (*1*)]. The 2003 Planetary Decadal Survey ranked exploration of the Kuiper Belt at the top of funding priorities for NASA s planetary program (*2*). The resultant NASA mission, New Horizons [e.g., (*3*)], flew through and explored the Pluto dwarf planet system in 2015 (*4*, *5*). The spacecraft has since continued farther to explore Kuiper Belt objects (KBOs) and the Kuiper Belt radiation and dust environment (*6*).

The target selected for the subsequent New Horizons KBO flyby was (486958) 2014 MU_{69} (hereafter MU_{69}, also informally referred to as Ultima Thule). This KBO was discovered in 2014 when the Hubble Space Telescope (HST) was being used to conduct a dedicated search for New Horizons KBO flyby targets (*7*, *8*). Before the arrival of New Horizons, the only definitive facts regarding MU_{69} were its orbit (*8*), its red color (*9*), its size of ~30 km (*7*), and its lack of

[1]Southwest Research Institute, Boulder, CO 80302, USA. [2]Johns Hopkins University Applied Physics Laboratory, Laurel, MD 20723, USA. [3]Southwest Research Institute, San Antonio, TX 78238, USA. [4]Lowell Observatory, Flagstaff, AZ 86001, USA. [5]NASA Ames Research Center, Space Science Division, Moffett Field, CA 94035, USA. [6]Department of Physics and Astronomy, University of Texas, San Antonio, TX 78249, USA. [7]Department of Earth and Planetary Sciences and McDonnell Center for the Space Sciences, Washington University, St. Louis, MO 63130, USA. [8]Department of Astronomy, University of Virginia, Charlottesville, VA 22904, USA. [9]Independent consultant, Carbondale, CO 81623, USA. [10]Universität der Bundeswehr München, Neubiberg 85577, Germany. [11]Laboratory for Atmospheric and Space Physics, University of Colorado, Boulder, CO 80303, USA. [12]NASA Goddard Space Flight Center, Greenbelt, MD 20771, USA. [13]KinetX Aerospace, Tempe, AZ 85284, USA. [14]SETI Institute, Mountain View, CA 94043, USA. [15]Planetary Science Institute, Tucson, AZ 85719, USA. [16]Jet Propulsion Laboratory, California Institute of Technology, Pasadena, CA 91109, USA. [17]Earth and Planetary Science Department, University of California, Santa Cruz, CA 95064, USA. [18]Massachusetts Institute of Technology, Cambridge, MA 02139, USA. [19]Argelander-Institut für Astronomie, University of Bonn, Bonn D-53121, Germany. [20]Rheinisches Institut für Umweltforschung, Universität zu Köln, Cologne 50931, Germany. [21]Lunar and Planetary Laboratory, University of Arizona, Tucson, AZ 85721, USA. [22]Department of Physics, University of Central Florida, Orlando, FL 32816, USA. [23]Cornell University, Ithaca, NY 14853, USA. [24]Independent science writer, Arlington, VT 05250, USA. [25]Pinhead Institute, Telluride, CO 81435, USA. [26]University of Idaho, Moscow, ID 83844, USA. [27]Department of Earth and Planetary Sciences, Birkbeck, University of London, London WC1E 7HX, UK. [28]University Grenoble Alpes, Centre National de la Recherche Scientifique, Institut de Planétologie et d Astrophysique de Grenoble, 38000 Grenoble, France. [29]NASA Headquarters, Washington, DC 20546, USA. [30]Department of Astronomy, University of Maryland, College Park, MD 20742, USA. [31]Department of Environmental Sciences, University of Virginia, Charlottesville, VA 22904, USA. [32]National Research Council of Canada, Victoria, BC V9E 2E7, Canada. [33]Division of Geological and Planetary Sciences, California Institute of Technology, Pasadena, CA 91125, USA. [34]Marine, Earth, and Atmospheric Sciences, North Carolina State University, Raleigh, NC 27695, USA. [35]National Optical Astronomy Observatory, Tucson, AZ 26732, USA. [36]NASA Marshall Space Flight Center, Huntsville, AL 35812, USA. [37]Independent consultant, Mountain View, CA 94043, USA. [38]Independent consultant, Crested Butte, CO 81224, USA. [39]Independent collaborator, Windlesham GU20 6YW, UK. [40]Department of Astrophysical Sciences, Princeton University, Princeton, NJ 08544, USA. [41]Stellar Solutions, Palo Alto, CA 94306, USA. [42]Independent consultant, Holland, MI 49424, USA. [43]Lunar and Planetary Institute, Houston, TX 77058, USA. [44]Space Telescope Science Institute, Baltimore, MD 21218, USA. [45]Johns Hopkins University, Baltimore, MD 21218, USA. [46]Roane State Community College, Oak Ridge, TN 37830, USA. [47]George Mason University, Fairfax, VA 22030, USA. [48]Independent consultant, Burden, KS 67019, USA.
Corresponding author. Email: astern@boulder.swri.edu

detectable variations in its light curve (*10*) or large, distant satellites.

MU_{69} s orbit has a semimajor axis a = 44.6 astronomical units (AU), with eccentricity e = 0.042 and inclination i = 2.45°, making it a member of the cold classical KBO (CCKBO) population (here, cold refers to low dynamical excitation, not surface temperature). CCKBOs are thought to be (i) distant relics formed from the Solar System s original protoplanetary disk and (ii) more or less dynamically undisturbed bodies that therefore formed in situ ~4.5 billion years ago and have since remained at or close to their current, large heliocentric distances (*11*, *12*). Relative to other Kuiper Belt populations, CCKBOs have a more uniformly red color distribution [e.g., (*13*)], as well as a different size-frequency distribution (i.e., the population of objects as a function of object size) (*14*) and higher average visible albedos than are typical in the Kuiper Belt [e.g., (*15*)]. Additionally, many CCKBOs have satellites (*16*).

Because CCKBOs are dynamically undisturbed from their formation location [or nearly so (*12*)], they have never been warmed above the ambient, radiative equilibrium temperatures of 30 to 60 K in the Kuiper Belt. MU_{69} s small equivalent spherical diameter of ~19 km is insufficient to drive internal evolution long after its formation. Therefore, small CCKBOs like MU_{69} are expected to be primordial planetesimals, preserving information on the physical, chemical, and accretional conditions in the outer solar nebula and the processes of planetesimal formation [e.g., (*1*, *12*)].

New Horizons flew closest to MU_{69} at 05:33:22.4 (±0.2 s, 1σ) universal time (UT) on 1 January 2019. The closest approach distance of 3538.5 ± 0.2 (1σ) km was targeted to the celestial north of MU_{69} s center; its relative speed past MU_{69} was 14.43 km s^{-1}. The asymptotic approach direction of the trajectory was approximately in the ecliptic plane at an angle of 11.6° from the direction to the Sun. The flyby s observation planning details have been summarized elsewhere (*6*). This report of initial flyby results is based on the ~10 of all collected flyby data that had been sent to Earth before 1 March 2019; full data transmission is expected to complete in mid-2020.

New Horizons carries a suite of seven scientific instruments (*3*); all were used in the flyby of MU_{69}. These instruments are (i) Ralph, which consists of the Multispectral Visible Imaging Camera (MVIC), a multicolor/panchromatic mapper, and the Linear Etalon Imaging Spectral Array (LEISA), an infrared (IR) composition mapping spectrometer; (ii) the Long Range Reconnaissance Imager (LORRI), a long–focal length panchromatic visible camera; (iii) the Alice extreme/far ultraviolet mapping spectrograph; (iv) a Radio Experiment (REX) to measure surface brightness temperatures and X-band radar reflectivity; (v) the Solar Wind Around Pluto (SWAP) charged-particle solar wind spectrometer; (vi) the Pluto Energetic Particle Spectrometer Science Investigation (PEPSSI) MeV charged-particle spectrometer; and (vii) the Venetia Burney Student Dust Counter (VBSDC), a dust impact detector.

General properties

MU_{69} (Fig. 1) has a bilobate shape with two discrete, unequally sized lobes. This shape demonstrates that it is a contact binary—that is, a pair of formerly separate objects now in physical contact with one another. These two lobes contact at an annular interface with higher than average surface reflectance, which we refer to as MU_{69} s neck. The larger and smaller lobes of MU_{69} have been informally designated "Ultima" and "Thule," respectively; formal names will be assigned at a later date.

The bilobate nature of MU_{69} is reminiscent of known bilobate comets that have been imaged by spacecraft (*17*–*22*). However, MU_{69} s residence in the cold classical Kuiper Belt makes clear that its bilobate shape must be primordial, making MU_{69} the only unquestionably primordial contact binary so far explored by spacecraft.

MU_{69} s two lobes are discrete, have retained their basic shapes, and do not (at the available resolution) display prominent compression features, deformation, or other geological features indicative of an energetic or violent merger. All available evidence indicates that MU_{69} is instead the product of a gentle collision or merger of two independently formed bodies, possibly contacting one another at (or more slowly than) their mutual gravitational infall speed, which we estimate to be several meters per second (based on plausible densities; see below).

The observed bilobate shape is inconsistent with a recent formation from the collision of two separate, heliocentric CCKBOs because the characteristic relative impact speeds of CCKBOs are currently ~300 m s^{-1} (*23*). Such a collision would have heavily deformed or destroyed the two components of the contact binary. We conclude that the lobes instead most likely formed and merged in a gentle dynamical environment, such as in a localized particle cloud collapse early in Solar System history [e.g., (*24*, *25*)], further indicating that MU_{69} itself is primordial. The similarity in albedos and colors of the two lobes (discussed below) is further evidence for this formation hypothesis.

Images taken during the approach phase show that the rotational period of MU_{69} is 15.92 ± 0.02 hours; this period is consistent with other CCKBO rotational periods (*9*, *26*, *27*). MU_{69} s rotational pole was found to point at approximately right ascension = 311°, declination = −25°, corresponding to an obliquity of 98° with respect to MU_{69} s heliocentric orbital plane; that is, MU_{69} currently rotates almost face-on to the Sun. This pole position, and the fact that the spacecraft approach vector was only ~36° from the direction of the KBO s spin axis, resulted in a light curve of very low amplitude, which was not detected until shortly before the flyby despite many weeks of prior observations from New Horizons. Because asymmetric reradiation (i.e., YORP, or Yarkovsky-O Keefe-Radzievskii-Paddack) effects are ineffective on bodies the size of MU_{69} at large distances from the Sun (*28*, *29*), and because (as described below) the visible evidence for impact cratering on MU_{69} is modest, the spin period and obliquity of MU_{69} are unlikely to have substantially changed since the binary merger.

We simultaneously fitted the shape of MU_{69} and its pole position using a forward-modeling process. For each of the early-return LORRI and MVIC images in which MU_{69} was resolved, this process rendered the shape with the relevant illumination and orientation using the photometric parameters described below, convolved that rendered image with the appropriate point-spread function (for LORRI or MVIC, as appropriate) to simulate the angular resolution and smearing of the real images, and then numerically compared the result to all of the resolved images of MU_{69} that had been returned. The shape model was parametrically defined, separately for each lobe, using the "octantoid" formalism (*30*) (see methods). Our best-fitting shape model (Fig. 2) has overall dimensions of approximately 35 × 20 × 10 km, with estimated uncertainties of less than 1 × 1 × 3 km. The thickness (i.e., the third dimension) is the least

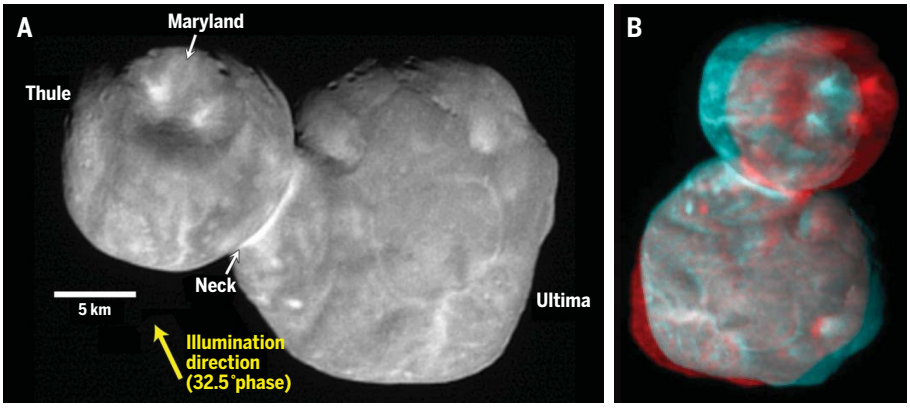

Fig. 1. Close approach 06 CA06) MVIC observation of MU_{69}. (**A**) MVIC image made at a solar phase angle of 32.5°, a range of 6640 km, and a native pixel scale of 130 m per pixel, resampled to a 2× finer pixel scale and then deconvolved using a similarly resampled MVIC point-spread function. (**B**) Red-cyan stereographic anaglyph of the MU_{69} approach hemisphere.

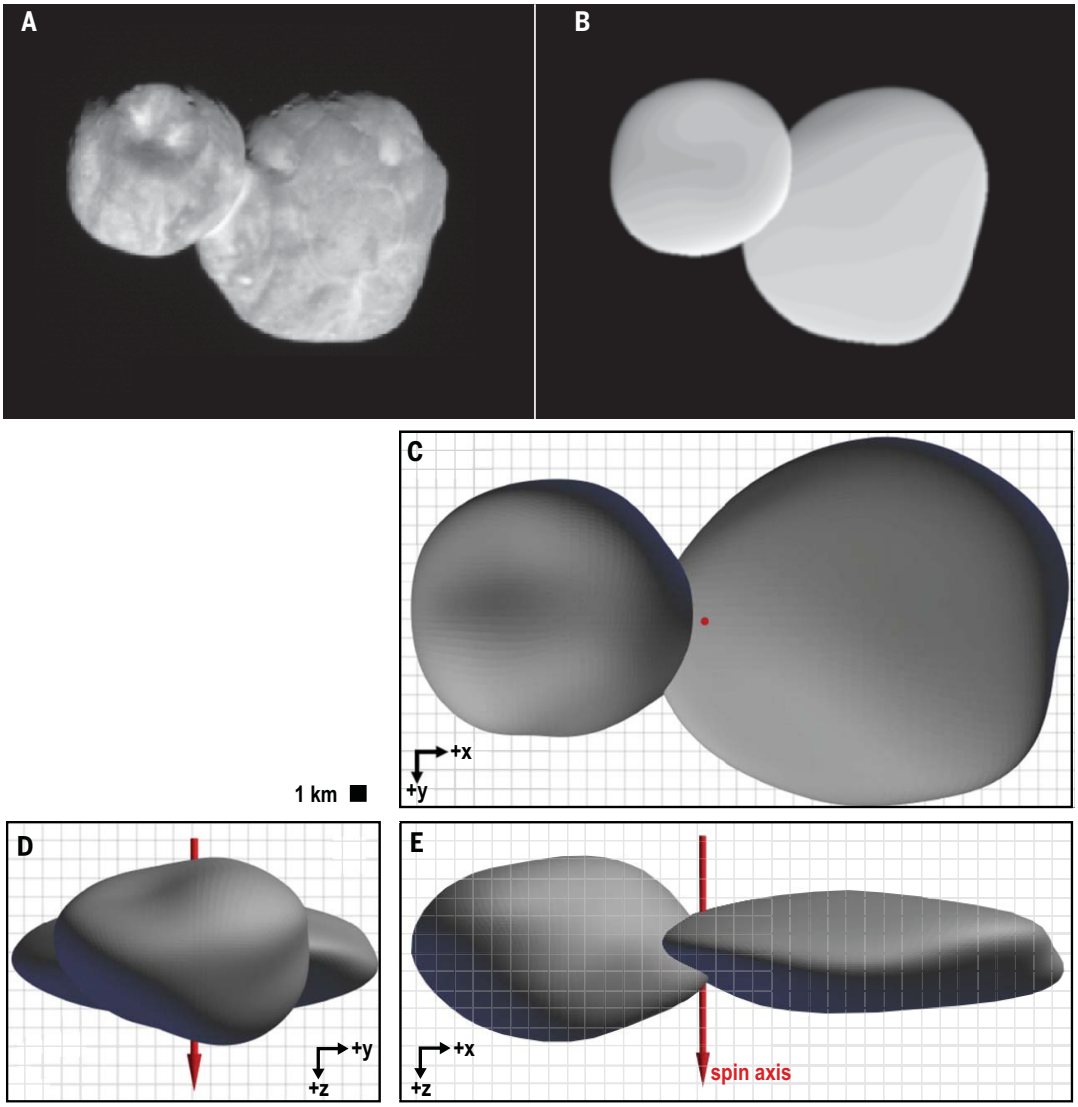

Fig. 2. Shape model for MU_{69}. (**A**) The same MVIC image as Fig. 1A for comparison. (**B**) Shape model of MU_{69} based on approach rotational coverage and close flyby observations, seen at the same viewing and illumination conditions as (A). (**C** to **E**) Shape model seen along MU_{69} s *z* (C), *x* (D), and *y* (E) axes, with the object s spin axis indicated in red. The arrow of the spin axis is the positive (i.e., north) pole. The shape of the +*z* hemisphere, which was mostly in darkness during the encounter, is the least well constrained part of the shape model.

well constrained because the spacecraft approach was at a high negative (i.e., southern) latitude on the object, so little of the positive (i.e., northern) half of MU_{69} was directly observed.

From this shape model, the Ultima lobe was found to be lenticular with dimensions of approximately 22 × 20 × 7 km (uncertainty < 0.6 × 1 × 2 km), whereas the Thule lobe is more equidimensional, approximately 14 × 14 × 10 km (uncertainty < 0.4 × 0.7 × 3 km). The model volumes of Ultima and Thule are 1400 km^3 (± <600 km^3) and 1050 km^3 (± <400 km^3), respectively. The centers of the lobes are 16 km apart. The principal axes of the lobes are roughly parallel to one another (likely <7° misalignment), which strongly suggests that the lobes tidally locked prior to contact (see below).

The apparently lenticular shape of the Ultima lobe is unlike any other known heliocentrically orbiting Solar System body, but is reminiscent of some small ring satellites of Saturn, such as Atlas and Pan, which have accreted equatorial ridges of fine-grained material (*31*). The origin of this flattened shape of Ultima is indeterminate; possible explanations include accretion from a thin (i.e., flattened) particle sheet during pebble cloud collapse (*24*), the head-on collision of two very similarly sized bodies within a narrow range of speeds (*32*), or deformation arising from rapid rotation or tidal forces prior to its merger with Thule. These possibilities are discussed below.

Because no satellites of MU_{69} were detected (see below), MU_{69} s density is poorly constrained. Cometary nuclei are the Solar System bodies likely to be most similar to MU_{69}; they are generally found to have low density (<10^3 kg m^{-3}) and high porosity (>50) (*21*). The most precisely determined comet nucleus density is that of 67P/Churyumov-Gerasimenko, at 533 ± 6 kg m^{-3} (*33*), although it is unknown how much that comet s density has evolved from its primordial value. Adopting the shape model in Fig. 2, a lower bound on MU_{69} s density of ~280 kg m^{-3} can be derived by assuming that MU_{69} s two lobes are only marginally bound by self-gravity and there is no tensile strength in the neck. Alternatively, assuming a characteristic cometary density of 500 kg m^{-3} (*21*) gives a breakup rotation rate for MU_{69} of ~12 hours. At this density, if the two lobes merged from a mutual circular orbit, substantial loss of angular momentum would have been required to reach their current, 15.92-hour period. Because mutual gravity would exceed centrifugal acceleration, densities greater than ~280 kg m^{-3} also imply that the neck region is currently under compression.

We calculated the gravitational and rotational potential across the surface of MU_{69} assuming the shape model in Fig. 2, a uniform density of 500 kg m^{-3}, and its 15.92-hour rotation period. The surface acceleration ranges between 0.5 and 1 mm s^{-2} (and is nowhere negative). The local acceleration slopes (i.e., the gradients of the gravitational and rotational potential across the surface) are low except in the neck, where they can exceed 35°. The equators of Ultima and Thule are gravitational and rotational potential highs.

Surface reflectivity, color, and composition

Figure 3A shows a visible-wavelength *I F* (reflected intensity divided by incident flux) contour map from the close approach 04 (CA04) LORRI observation (13° solar phase angle) and its corresponding *I F* histogram. At this solar phase angle, the modal *I F* of MU_{69} is 0.078. The *I F* distributions of MU_{69} s two lobes have the same mode within the measurement error of ±0.05 *I F*. *I F* variations ranging from ~0.02 to ~0.12 are seen on both lobes (including their terminator regions). However, away from the terminator (i.e., the surface boundary between daylight and nighttime where lighting effects bias results), the minimum *I F* is ~0.05. This occurs on a portion of the wall of the large depression on Thule, which we informally refer to as Maryland (surface features on Ultima Thule are informally named after U.S. states with major contributions to New Horizons); see Fig. 1. The maximum *I F* of ~0.12 occurs at both of the bright spots in Maryland and on the neck region. The *I F* distribution of the Ultima lobe has a sharper peak than that of Thule (Fig. 3B).

The brighter material on Ultima and Thule is mostly segregated into three kinds of surface manifestations: (i) nearly circular spots that become more numerous with decreasing size (ranging from a few kilometers across to the resolution limit of several tens of meters); (ii) curvilinear and quasi-linear features that are narrow relative to their length; and (iii) broad patches, which are more prominent on the Thule lobe. Darker than average surface units on the binary also come in types (i) and (iii), but not (ii).

It is unclear how these three types of comparatively bright terrain originated and how they may differ. However, initial stereographic analysis of New Horizons images using established techniques (*34*, *35*) shows that many of the observed bright areas on MU_{69} are located either within topographic depressions (e.g., the neck, the bright spots in Maryland, and the floors of pits and troughs) or at the bases or inflection points of slopes. Therefore, a possible explanation is that bright, fine-grained material has been transported downslope to these locations, in which case the higher brightness could be due to predominantly smaller particle size (*36*). However, other interpretations including compositional or thermal effects, space weathering, and cold trapping are also possible.

The neck feature at the Ultima-Thule merger zone might not have the same origin as other bright locales. Possibilities include (i) surface processes such as fine particle accumulation, as discussed above; (ii) processes related to the lobe merger, such as the extrusion of preexisting bright surface material on one lobe during the impact; (iii) post-impact thermal extrusion of ices due to changes in thermal properties or conditions at the merger zone after contact; and (iv) evolutionary processes such as preferential space-weathering effects or thermal effects created by the geometry surrounding the neck.

Analyses of the approach and departure images have allowed us to characterize the solar phase curve of MU_{69} at phase angles up to 153°, considerably higher than possible for Earth-based observations of this object, which are limited to ~2° (Fig. 4). The derived phase coefficient, or slope, is β = 0.038 ± 0.014 magnitudes per degree, between 1.3° and 32.5°. This slope is consistent with that measured for other low-albedo small Solar System bodies, including comet nuclei [e.g., (*37*)]. Applying a Hapke photometric model (*36*) to the entire phase curve yields the nominal photometric properties of MU_{69} s surface: single scattering albedo ω_o = 0.24, mean topographic slope angle θ = 33°, and single-particle phase function parameters using a McGuire-Hapke formalism (*37*) of *b* = 0.32 and *c* = 0.75. These results give MU_{69} s visible (0.55-μm *V*-band) geometric albedo (i.e., the albedo at 0° solar phase) of p_V = 0.165 ± 0.01. This is a typical value for CCKBOs, the geometric albedos of which range from 0.09 to 0.23, with a mean of 0.15 (*38*). MU_{69} s phase integral is *q* = 0.37 ± 0.16, yielding a spherical (Bond) albedo of 0.061 ± 0.026.

MVIC color images reveal a globally averaged visible-wavelength reddish reflectance slope of 31.1 ± 0.5 per 100 nm, computed using MVIC s blue, red, and near-IR filters (Fig. 5, A to C), where the quoted uncertainty here is statistical only. This color is consistent with that of other CCKBOs (*39*–*41*). Only subtle color (and spectral; see below) differences (and spectral differences; see below) are detected between the two lobes of MU_{69}, despite their distinct shapes and appearances. The two lobes are clearly resolved from one another at the resolution of the color data. Remote observations of KBOs with satellites show near-equal colors of the orbiting bodies, interpreted as resulting from co-accretion from a locally homogeneous portion of the nebula (*42*).

The clearest regional color and spectral signatures across MU_{69} s surface appear (i) at the neck between the two lobes, and (ii) at the Thule lobe bright spots in Maryland, which display spectral slopes of 28.2 ± 0.2 per 100 nm and 30.8 ± 0.2 per 100 nm, respectively. At least two locations on the Ultima lobe also show less red than its average color. Principal components analysis shows that 97 of the variance in MVIC color data is attributable to shading and albedo, whereas image noise and true color contrasts account for just 3 . The subtle color differences seen could be indicative of compositional differences, although differences in particle size, porosity, etc., can also produce differences in spectral slopes.

LEISA spectral observations (Fig. 5D; see methods) show that MU_{69} is brighter in the near-IR than it is in the visible spectrum, demonstrating that the red slope observed using MVIC extends into the IR. From 1.2 to 2.5 μm, the observed *I F* after radiometric calibration ranges from 0.15 to 0.2. The colorant responsible for the redness of MU_{69} and other CCKBOs could be tholin-like complex organic macromolecules, produced from simpler species through radiolytic and photolytic breaking of bonds leading to recombination into progressively heavier molecules [e.g., (*43*, *44*)]. Space weathering of silicates can also produce a red coloration, but no direct evidence of silicates is seen on MU_{69}. Principal components analysis shows that more than 90 of the variance in the LEISA data is also due to shading and albedo, with relatively little variance attributable to regional spectral variability.

As shown in Fig. 5D, there are key color slope similarities between the spectrum of MU_{69} and

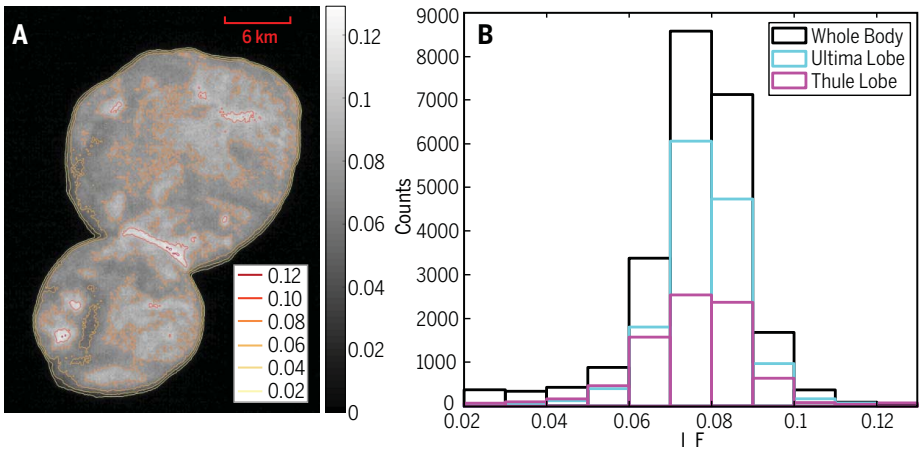

Fig. 3. Albedo contour map and histogram for the CA04 LORRI observation. (**A**) *I F* isocontours of light scattered from MU_{69} s surface at 13° solar phase angle. (**B**) Histogram of *I F* pixel values; these *I F* values refer to the LORRI pivot wavelength (607.6 nm). The spectral distribution of MU_{69} was approximated as a 50 Pluto plus 50 Pholus spectrum (see text).

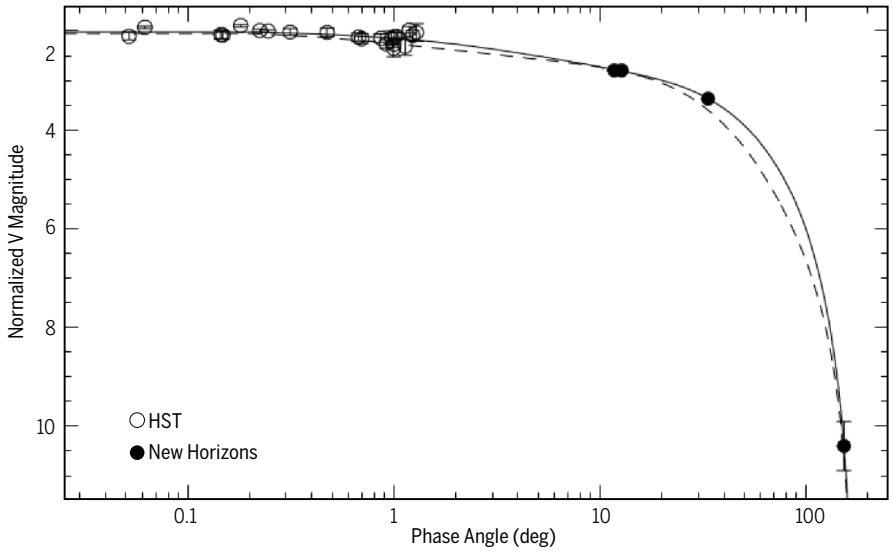

Fig. 4. The visible 0.55 m) solar phase curve of MU_{69} obtained by combining HST and New Horizons data. The solid line is the Hapke photometric model (*82*) fitted to the total integrated *I F* of MU_{69}. Data are from New Horizons close approach images acquired at solar phase angles of 12°, 13°, 32.5°, and 153° and from observations by the HST at low phase angles (<1.3°). Error bars on the 153° observation primarily arise from uncertainty in the shape of MU_{69} s night side. Magnitudes are normalized to the geometric albedo (p_V = 1) at opposition (α = 0°) in the *V* band (0.55 μm); no corrections have been made to account for rotational variation in reflectance (i.e., the light curve), but MU_{69} s light curve amplitude upper limit is low [0.15 magnitudes (*10*)], so this neglected effect is small. For comparison, the dashed line is the solar phase curve of 103P/Hartley 2 (*83*), a bilobate Jupiter family comet visited by the Deep Impact spacecraft (*84*). Although Hartley 2 is darker (p_V = 0.045 ± 0.009) than MU_{69} at 0.55 μm, the phase curves of these two bodies have similar shapes.

those of the KBO (55638) 2002 VE_{95} (*45*) and the escaped KBO 5145 Pholus [e.g., (*46*)]. Also, these objects all exhibit an absorption band near 2.3 μm, tentatively attributed to methanol (CH_3OH) or perhaps more complex organic molecules intermediate in mass between simple molecular ices and tholins (*47*). Similar spectral features are also apparent on the large, dark red equatorial region of Pluto informally called Cthulhu [e.g., (*48*)], suggesting similarities in the chemical feedstock and processes that could operate there and on MU_{69}.

Broad spectral absorption features on MU_{69} near 1.5 and 2.0 μm indicate the presence of H_2O ice. However, the shallowness of these features suggests that water ice may have a relatively low abundance in MU_{69} s uppermost surface, at least compared with water ice–rich planetary satellites, and even on Pholus and in Cthulhu where H_2O ice is more clearly detected. In this regard, opaque species such as complex organics are known for their ability to mask the spectral signature of H_2O ice in the near-IR (*49*). No unambiguous spectral signatures of silicates, or of volatile ices like those that were observed on Pluto (CO, N_2, NH_3, or CH_4) (*4*), have been detected for MU_{69}, but most of these supervolatile species are not expected at MU_{69} owing to the ready thermally driven escape of such ices from this object over time. An apparent absorption at 1.8 μm has not yet been assigned a molecular identification.

Thermal considerations

Temperatures on MU_{69} are set by the balance between the absorption of sunlight and thermal emission back to space. For the 6 Bond albedo estimated above, and an assumed 90 emissivity, absorption and emission at MU_{69} s mean distance from the Sun are balanced at 42 K. For plausible values of thermal conductivity in the 10^{-5} J m^{-1} s^{-1} K^{-1} range, we estimate the characteristic skin depths to which diurnal and seasonal waves propagate to be ~0.001 m and ~1 m, respectively (see methods). Therefore, diurnal and seasonal temperature variations likely only affect the outer few millimeters to meters of MU_{69} s surface, so the average temperature pertains to the vast majority of MU_{69} s interior. At this 42 K temperature, frozen volatile species such as CO, N_2, and CH_4 not trapped in clathrates would sublimate and escape relatively rapidly compared to the age of the Solar System, but amorphous H_2O ice would not crystallize and so could survive over the age of the Solar System.

Near the surface of MU_{69}, temperature varies on seasonal and diurnal time scales. As a result of MU_{69} s low orbital eccentricity, insolation only differs by 17 over the course of its orbit. However, summer/winter hemisphere insolation varies considerably over MU_{69} s 293-year orbit because of the 98° obliquity of its pole, resulting in long polar days and nights during which regions receive continuous sunlight, or none at all, for many decades. Around equinox, the 15.92-hour rotation period would also produce strong diurnal variations in insolation. Changing insolation generates thermal waves as heat is conducted into and out of the subsurface.

We expect summer surface temperatures to approach a maximum instantaneous equilibrium temperature of ~60 K, whereas winter temperatures (as on the unilluminated face of MU_{69} during the New Horizons flyby) are much lower, down to the seasonal skin depth. Analysis of the REX radiometry data at the 4.2-cm X-band radio wavelength indicates a brightness temperature in the 20 to 35 K range on the winter (night) side of MU_{69}. Thermal emission at centimeter wavelengths emerges from a range of depths, potentially up to many tens of wavelengths below the surface, so the warmer subsurface is an important source of flux. For typical icy satellite emissivity at centimeter wavelengths (*50*, *51*), the observed REX brightness temperature range appears to be consistent with the expected low thermal inertia values estimated for other KBOs (*52*).

Geophysical and geological properties

We measured the limb profile of MU_{69} using previously published techniques (*53*). These limb profiles (Fig. 6, A and B) were derived from the CA04 LORRI (characteristic 140 m per pixel) and CA06 MVIC (characteristic 130 m per pixel) observations and were compared with best-fitting ellipses for the projected shape of each lobe. The elliptical axes remove the long-wavelength signal and are not necessarily representative of the 3D body shape (i.e., they are not measured with respect to the shape model in Fig. 2).

On the larger lobe Ultima, the limb topography shows total (i.e., minimum to maximum deviation) relief of ~1 km, whereas the relief on the smaller lobe Thule is more muted at ~0.5 km. Assuming a density ρ = 500 kg m^{-3}, a surface gravity g = 0.001 m s^{-2}, and topography of vertical scale h = 0.5 to 1 km implies stresses on the order of $\rho g h/3$, or ~100 Pa. Such modest stresses can be supported by friction. Excessively steep regions (>35°) near MU_{69} s neck likely require additional internal strength to remain stable. Cohesion of several hundreds of pascals would be capable of supporting these slopes. Such strengths are thought to be normal for comet-like bodies (*22*) and so are plausible for KBOs of MU_{69} s size as well.

A geomorphological map of MU_{69} is shown in Fig. 6C. The two lobes have somewhat different surface geology. Thule s surface is dominated by Maryland, a depression of probable impact origin (unit labeled *lc*; see Fig. 6C for key to these abbreviations), ~7 km in diameter (see above). Stereographic analysis shows that the depth of Maryland is <2 km; this depth is consistent with the observed limb topography variations. Maryland s interior shows no unambiguous signs of horizontal layering but does contain two prominent bright spots of similar size and albedo. Two distinct, kilometer-scale, possible impact craters occur on Maryland s rim crest. Separately, four distinct troughs appear near the terminator of Thule in unit *um*.

Apart from Maryland, the rest of Thule s observed surface is characterized by broad (few kilometers wide), dark swaths (unit *dm*) that separate lighter-toned, mottled units (units *pm*, *um*, and *rm*). In some places, these dark swaths contain bright spots and a bright-floored, quasi-linear

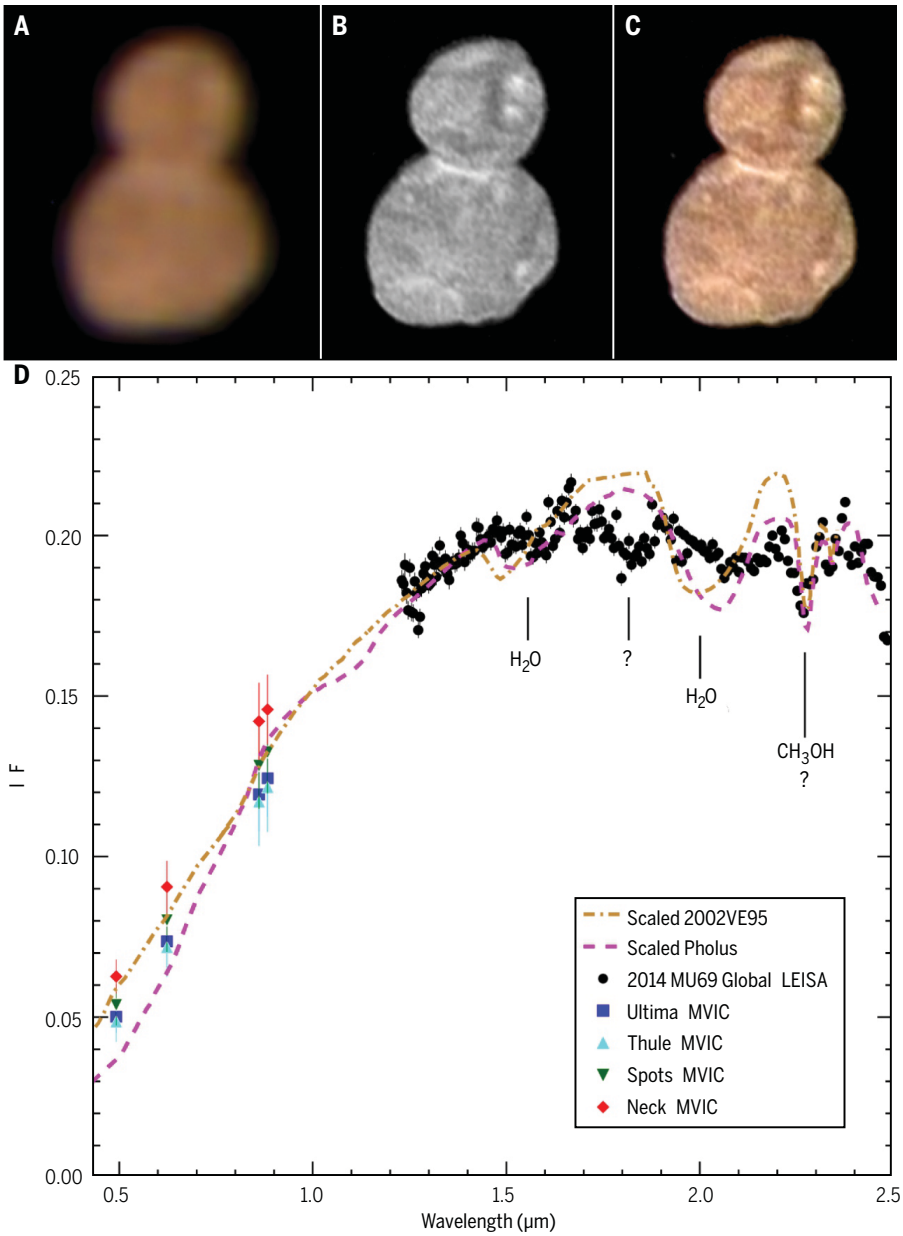

Fig. 5. MU_{69} s color and near-IR spectral reflectance. (**A**) MVIC enhanced color image at a scale of 1.5 km per pixel. (**B**) CA04 LORRI image at 140 m per pixel. (**C**) (A) overlaid on (B). (**D**) MVIC color measurements (colored points) and a LEISA near-IR spectrum of MU_{69} (black points). Data at wavelengths shorter than 1 μm are from the MVIC visible/near-IR color imager at a phase angle of 11.7°; data at wavelengths longer than 1.2 μm are from the LEISA IR spectrograph at a phase angle of 12.6° and a mean spatial scale of 1.9 km per pixel. The MVIC data are split into multiple terrain units (Ultima and Thule lobes, the bright neck region, and a combination of all other bright spots identified in LORRI data); the LEISA spectrum is a global average. All LEISA data points illustrate an estimated 1σ uncertainty; MVIC data points illustrate an estimated 1σ uncertainty relative to the red channel flux. The data are compared to Hapke model spectra shown as the brown dot-dashed line of 2002 VE_{95} (*45*) and the magenta dashed line of 5145 Pholus (*46*). Those curves are scaled by 0.45 and 0.84, respectively, to match the average near IR *I* / *F* of MU_{69}. The apparent wavelength shifts of some features in the MU_{69} spectrum relative to the dashed models are likely due to unmodeled temperature, particle size, and temperature effects. Tentative identifications of absorption bands of water and methanol ices are marked, along with an unknown feature at 1.8 μm (see text).

trough. The crenulated boundaries of unit *dm* may be a decrescence morphology, whereby this unit is partly bounded by scarps that have retreated. Unit *dm* may be a deposit of volatile ice with bounding scarps forming as a result of sublimation at its periphery, with the upper surface of the deposit being protected from sublimation by a dark, refractory mantle, perhaps derived from the deposit itself (*54*, *55*). Portions of unit *um* that are proximal to Maryland may be ejecta from the crater, or related to ejecta, but this cannot be confirmed with the current analysis. A distinct, relatively bright region (unit *rm*) at the equatorial, distal end of Thule exhibits roughness at the scale of a few hundred meters; some of the features there appear to be pits, craters, or mounds.

A lightly cratered surface of MU_{69} was predicted by a recent cratering model (*23*); indeed, few definitively impact-related scars are identified on MU_{69}. We have considered several hypotheses for the origin of the many pits seen near the terminator in Fig. 2A. These include structurally controlled collapse pits, outgassing pits, sublimation pits, and impact craters (*56*); they likely are not all created by the same process. Our assessment is that the chains of similarly sized pits are more likely to be formed by internal processes than by cratering, but the isolated pits that show approximately circular planform outlines, bowl-shaped interior depressions, and, in some cases, raised rims are more consistent with impact crater morphology. There are no obvious crater candidates that are intermediate in size between these ~1-km-diameter pits (unit *sp*) and Maryland (unit *lc*, ~7 km).

On Ultima, eight similarly sized (~5 km scale) units of rolling topography (based on subtle albedo gradations and limb profiles) dominate its observed landscape (units *ma* to *mh*). The albedo and texture of these units are generally similar to one another, although each contains brighter material to differing degrees. These units abut each other, typically bordered with distinct, curvilinear, and generally higher-reflectance boundary regions (particularly unit *mh*, which is ringed by a brighter annulus). In one instance (near the terminator), a trough and a short pit chain mark such a boundary, but the low solar incidence angles prevailing across much of Ultima make it unclear whether the boundaries are always associated with topographic features. Stereographic analysis indicates that most of these units have broadly positive relief, although the central unit *mh* is relatively flatter. It is also unclear whether these boundaries necessarily imply superposition relationships among the components. One unit, at the limb of Ultima (unit *md*), appears to be more angular in stereography and is either more elevated or tilted with respect to the other components.

The apparent similarity in the size of Ultima s units (*ma* through *mh*) is likely a clue to their origin. Whether they are a relic of Ultima s formation or a result of a later evolution is unclear. One formation-related hypothesis is that the individual units on Ultima are accretional subunits of smaller planetesimals that formed Ultima. This apparent assemblage of units on Ultima is consistent with observation of and proposals for the formation of layers on comets such as 9P/Tempel and 67P/Churyumov-Gerasimenko (*20*, *57*). However, challenges to this hypothesis are the apparently (i.e., at the available resolution) nearly unimodal size of these units and their apparent absence from Thule, although the latter could be the result of resurfacing caused by the Maryland cratering event. Also, at the

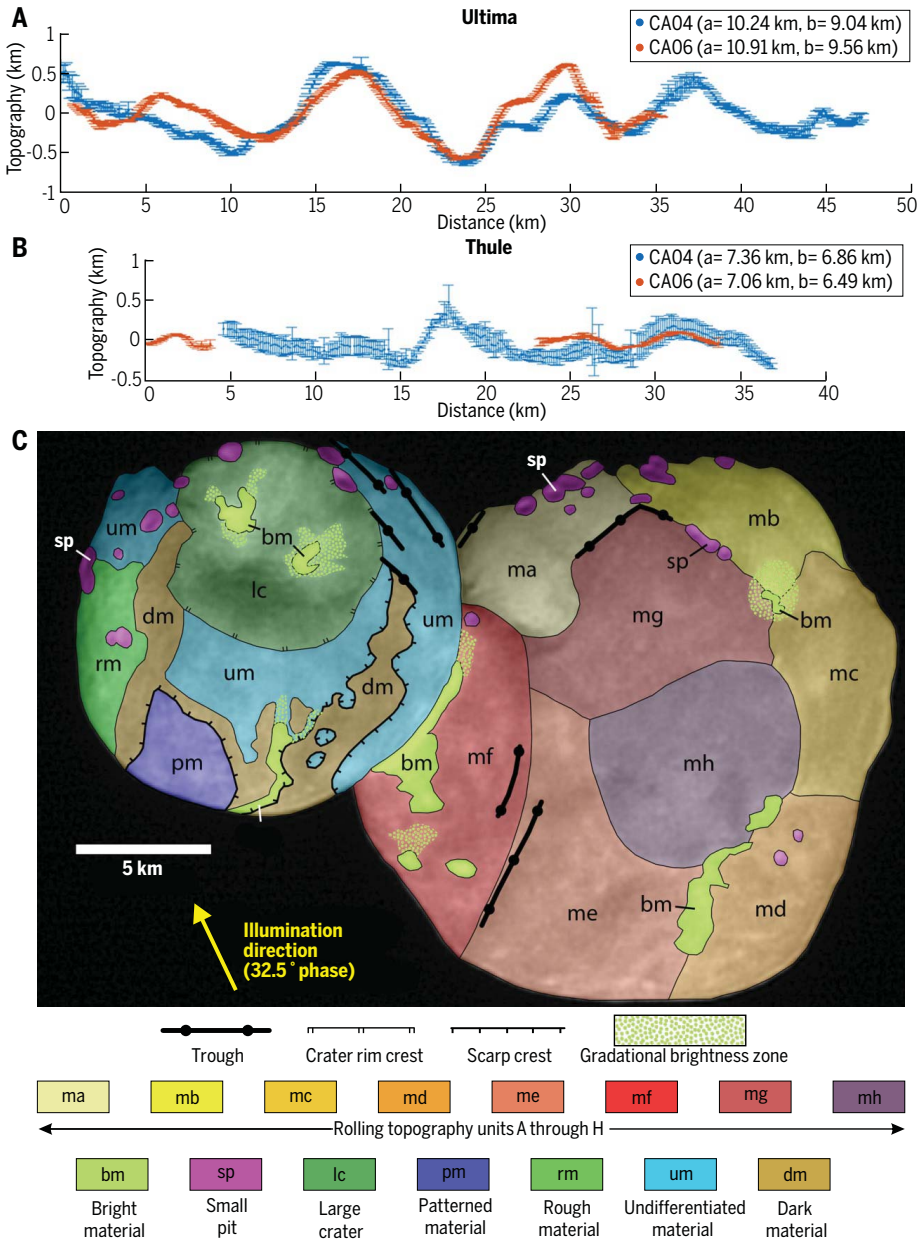

Fig. 6. Approach observation limb profiles and geomorphological map of MU_{69}. (**A** and **B**) Limb topography profiles of Ultima and Thule, respectively, measured using the LORRI CA04 and MVIC CA06 observations, after subtracting the best-fitting projected elliptical figures. The semimajor (A) and semiminor (B) axes of the best-fitting ellipses are indicated. Error bars represent the difference in estimated limb positions between two independent workers; the median difference was ~0.3 pixels for MU_{69} as a whole. The low solar phase angle of the CA04 observation (~12°) allows the limb to be measured more reliably around a larger portion of the perimeter of MU_{69} than for CA06 (solar phase 32.5°). (**C**) Geomorphological map of MU_{69}. The base map is the MVIC image from Fig. 2A. The positive spin axis of MU_{69} is pointing approximately into the page. The mapped boundaries are preliminary. Note that this mapping is physiographic in nature and is not intended to rigorously convey stratigraphic relations between units.

expected impact speeds during accretion, such as in a local particle cloud collapse resulting in a body like MU_{69} (perhaps no more than a few meters per second, based on the mutual escape speed of the lobes), these accretional subunits would likely not be expected to merge into as compact a body as Ultima unless they were extremely weak (i.e., cohesionless and frictionless) at the time of their accretion (*22*).

Satellites and orbiting rings/dust search

Both satellites and rings have been detected around KBOs larger than MU_{69} and around Centaurs (*16*, *58*, *59*), which have escaped the Kuiper Belt and now orbit among the giant planets. Although no KBO as small as MU_{69} is known to have rings, satellites around KBOs are common, particularly in the CCKBO population (*16*).

We searched for satellites and rings of MU_{69} using co-added stacks of LORRI images acquired during approach to MU_{69} at exposure times of 10 to 30 s. High-resolution images taken near closest approach provide additional constraints on satellites close to MU_{69}. No satellites were detected in our data. Figure 7A shows the quantitative limits on satellites obtained from these data as a function of distance from MU_{69}.

Additionally, small particles orbiting MU_{69} could form ring or other dust structures with unusual geometries (*60*) because MU_{69} s very weak gravity is of similar magnitude to the solar radiation pressure. However, larger grains, which are less affected by solar radiation pressure, could form a conventional equatorial ring (*60*).

Approach images constrain any ring or dust assemblages located 250 km from MU_{69} to have $I\,F \lesssim 2 \times 10^{-7}$ (for a 10-km-wide ring) at a phase angle of 11° (Fig. 7B). This is equal to or less than the $I\,F$ of many faint outer rings of the giant planets, which have ring widths of >20 km (*61*, *62*). A single downlinked high-phase (165°), forward-scattered observation also shows no evidence for rings or dust farther than ~400 km from MU_{69} at $I\,F > 10^{-4}$. The VBSDC dust counter experiment reported zero dust impact detections during the passage through the gravitational stability sphere of MU_{69}, consistent with a lack of extant rings or other dust assemblages.

Exosphere and heliospheric interaction searches

Because of MU_{69} s small size, it is likely that highly volatile ices that might once have been present at its surface would have escaped to space long ago (*6*, *56*). However, less volatile ices (e.g., methanol, acetylene, ethane, and hydrogen cyanide) could be retained over geological time scales, and irradiation of these species could result in reddening over time as longer-chain tholins are produced (*63*, *64*). This implies a slow loss of hydrogen atoms to space as surface ices are converted into tholins. In addition to this escaping H flux, occasional large impacts could provide a source for a transient atmosphere.

We searched for evidence of both a coma of escaping gas and charged particle emissions from MU_{69}. The searches included use of the Alice ultraviolet spectrograph to search for resonance line emission from a coma, as well as in situ searches for emitted MU_{69} ions with SWAP and PEPSSI.

An Alice count rate spectrum is shown in Fig. 8A. This observation was made over a period of 300 s, ~90 min before closest approach, from a range r ~ 80,000 km. We fitted a model to the spectrum including background emissions from interplanetary hydrogen plus four nearby stars. No coma emissions from MU_{69} were detected. At the brightest likely coma emission of the hydrogen 121.6-nm line, we find a 3σ upper limit

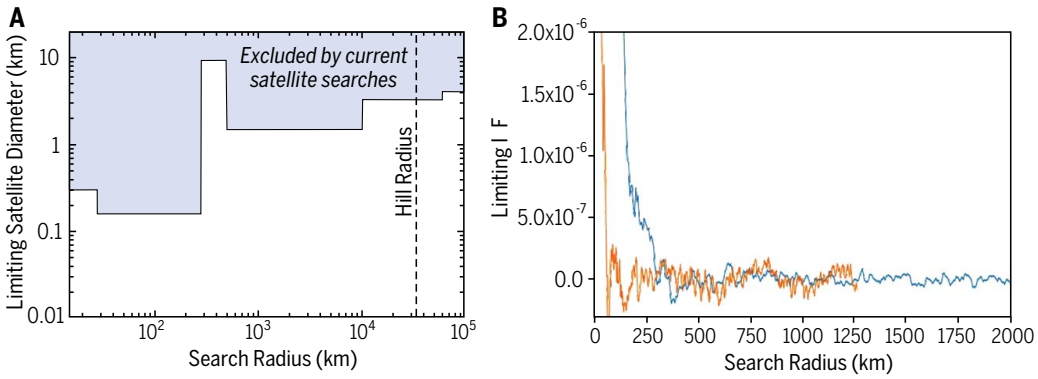

Fig. 7. Upper limits on satellites and ring/dust structures around MU_{69}. (**A**) Satellite search limiting diameters, assuming that satellites have reflectivity similar to that of MU_{69}. The Hill radius (i.e., maximum orbit stability radius against solar tides) shown here assumes an effective spherical-equivalent radius of 7.5 km for MU_{69} (approximating the lobes as ellipsoids) and a density of 500 kg m^{-3}. (**B**) Profiles of limiting ring detectability for *I F* versus distance from MU_{69}, assuming a 10-km-wide ring, obtained using LORRI observations made at 22 hours (blue) and 6.5 hours (orange) before closest approach. The increasing *I F* constraints inward of ~250 km are due to stray light from MU_{69} within LORRI s optics, not material around MU_{69}.

source rate of $<3 \times 10^{24}$ H atoms s^{-1} released by MU_{69}. Scattering of sunlight by H atoms at this source rate would produce a detectable emission, assuming a distribution that falls off as r^{-2} from MU_{69}.

No structured magnetic interaction between the solar wind and MU_{69} was expected because, at a typical interplanetary magnetic field of 0.2 nT, the gyro-radius of a proton picked up by the solar wind is $\sim 2 \times 10^4$ km; this distance is larger than MU_{69} by a factor of ~1000 and is also much larger than the flyby closest approach distance of ~3500 km. Shown in Fig. 8, B to E, are SWAP data taken during the time of the flyby. The bulk solar wind density and speed measured by SWAP near MU_{69} are ~2000 protons m^{-3} and ~425 km s^{-1}, respectively, for a solar wind flux of 8.5×10^8 protons m^{-2} s^{-1}. Variations are attributable to changes in spacecraft orientation relative to the solar wind, but there is no signature of any detected interaction of the solar wind with MU_{69}. Shown in Fig. 8, F to I, are PEPSSI data taken during the flyby, which also show no evidence of any MU_{69}-related signature. All PEPSSI variations in count rate are associated with spacecraft attitude changes, as with SWAP, and are consistent with an unperturbed interplanetary medium.

We can estimate the interaction that might be detected by SWAP or PEPSSI using the upper limit from Alice. For an outflow source rate of Q particles s^{-1}, the density at r is given by $n \sim Q/4\pi r^2 v$. For the Alice upper limit of $Q \sim 3 \times 10^{24}$ H atoms s^{-1}, the density at closest approach range is $\sim 2.4 \times 10^7$ H atoms m^{-3} (assuming the H atoms have a radial velocity $v \sim 800$ m s^{-1}, their thermal speed at 40 K). A fraction γ of those H atoms can become ionized and picked up by the solar wind to be detected by SWAP or PEPSSI. Then the count rate is $R = \varepsilon G n v_{SW} \gamma / 4\pi$, where ε is the detection efficiency near the solar wind speed, G is the instrument geometric factor, and v_{SW} is the solar wind speed. This indicates a PEPSSI count rate of $R \sim 8000\ \gamma$ counts s^{-1}. We estimate $\gamma \sim 2 \times 10^{-7}$ from the fraction of H atoms that could be photoionized by sunlight during the travel time $t \sim d_{CA}/v$ for H atoms to get from MU_{69} to the closest approach distance of New Horizons (d_{CA}); the expected PEPSSI count rate of 1.6×10^{-3} Hz would thus be smaller than the typical background count rate (~1 Hz) by a factor of ~600. A similar result is found for SWAP. Hence, the upper limit found with Alice data is more constraining than the SWAP and PEPSSI upper limits.

For comparison, we estimate the loss rate from photosputtering of water ice on MU_{69} to be $\sim 10^{19}$ H atoms s^{-1}, much less than our detection upper limit. This estimate is based on the combined direct solar and interplanetary medium H 121.6-nm flux at MU_{69} of 1.6×10^{12} photons m^{-2} s^{-1} and 4.0×10^{11} photons m^{-2} s^{-1}, respectively (*65*, *66*), and a yield of 0.003 for H 121.6-nm sputtering of water ice (*67*–*69*). Projected and total surface areas for MU_{69} of $\sim 4.1 \times 10^8$ m^2 and 1.7×10^9 m^2, respectively, were used in this estimate. Over 4.5 billion years, the water ice lost by this process would reduce the size of MU_{69} by a negligible ~0.01 m. Water ice is also eroded by solar wind ions (mainly protons), but this process is estimated to remove only about the same amount of material over time as the photosputtering (*70*).

Implications for formation

The New Horizons flyby has revealed many properties of MU_{69} but has also raised some puzzles. The latter include the origin of its two nonspherical and markedly different lobe shapes; the provenance of its brighter spots, zones, and linear/curvilinear features; the nature of the similarly sized surface units on Ultima; the degree to which the object is cratered; the origin of its bright neck; and how its two lobes formed and then merged to create the contact binary we observe.

Despite these puzzles, MU_{69} has already provided information on the ancient accretion processes that operated in the distant protosolar nebula and the Kuiper Belt (*71*, *72*). For example, MU_{69} lends weight to model predictions that binaries in the Kuiper Belt may have formed in local, low- to medium-velocity accretion clouds as in pebble cloud gravitational collapse models (*24*). The lack of strong surface albedo, color, and composition heterogeneity between the two lobes supports this hypothesis, because in a local pebble cloud collapse, MU_{69} s two lobes would form from a single source of material. However, it is also possible that material accreted throughout the cold classical Kuiper Belt may have been compositionally homogeneous to begin with.

The binary size ratios produced in existing pebble cloud collapse models (*24*), while focused on the formation of much more massive (100-km scale), co-orbiting binaries, are also consistent with the size ratio of the two lobes of MU_{69} (size ratio ≈ 0.75). Such models also produce appropriately low merger speeds (*24*, *25*) if they scale with the virial mass to much smaller clouds. However, MU_{69} s pole is highly inclined to the ecliptic, which is not a common outcome in cloud collapse models, given that the cloud s initial rotation state is set by heliocentric Keplerian shear. In contrast, turbulent particle concentration models, such as an overdense collection of swirling particles collapsing under the influence of aerodynamic drag in the protosolar nebula (*73*), have no preferred initial swirl (mean angular momentum) orientation.

Mechanisms fundamentally different from local pebble or particle cloud collapse have also been proposed for the formation of small-body binaries. However, some such mechanisms, such as YORP spin-up and fission (*28*, *29*), apply only in the inner Solar System where thermal radiation forces are sufficiently strong. In the outer Solar System, binary systems may instead form via three-body exchange capture (*74*), but such mechanisms require heliocentric encounter velocities generally near or lower than the Hill speed [the heliocentric Keplerian shear speed at the limit of the primary body s gravitational sphere of influence (*24*)], which for MU_{69} would have been an implausibly low ~1 cm s^{-1}; hence, such models are disfavored. We also do not favor this three-body formation mechanism because binaries formed by such three-body exchange would likely rotate either prograde or retrograde (*24*, *75*), not highly obliquely like MU_{69}.

For MU_{69} s two lobes to reach their current, merged spin state, they must have lost angular momentum if they initially formed as co-orbiting bodies. The lack of detected satellites of MU_{69} may imply ancient angular momentum sink(s) via (i) the ejection of formerly co-orbiting smaller bodies by Ultima and Thule, (ii) gas drag, or

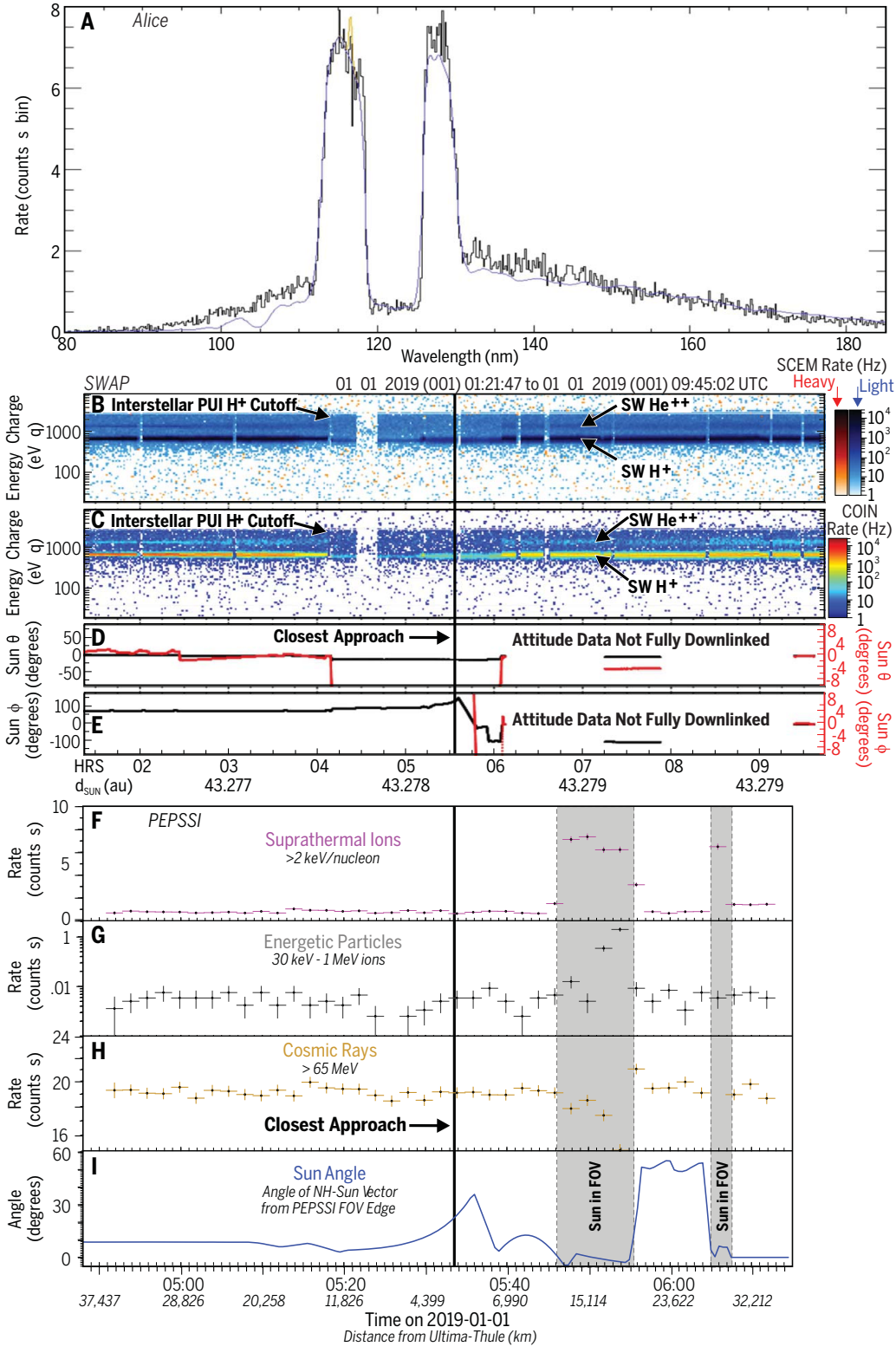

Fig. 8. MU_{69} atmospheric and plasma search results. (**A**) Alice ultraviolet airglow spectrum. A modeled background (blue) includes interplanetary H emissions and four nearby stars. A small model signal at 116.6 nm (gold) indicates the H 121.6 nm count rate that would be expected if MU_{69} were outgassing H atoms at $Q \sim 3 \times 10^{24}$ atoms s^{-1}; the 121.6-nm H signal appears at this wavelength because the observations were offset to avoid a low-sensitivity region of the detector. No MU_{69} coma emission is detected in the observed spectrum (black). (**B** and **C**) SWAP low-energy plasma spectrometer data showing light (blue) and heavy (orange) secondary channel electron multiplier (SCEM) count rate energy/charge spectra, where light (i.e., H^+ and He^{++}) and heavy ions are distinguished by their low and high secondary/primary electron ratios as they pass through SWAP s carbon foil (*65*), and coincidence rates (COIN) spectra. The heavy ions are sparse and are not associated with close approach. (**D** and **E**) SWAP orientation with respect to the Sun in altitude (θ) and azimuth ( ) angles (black, full range; red, zoomed). All the changes observed in the coincidence rate spectra in (B) and (C) are associated with changes in spacecraft orientation; no changes related to the presence of MU_{69} were observed. (**F** to **I**) PEPSSI energetic particle spectrometer data. Count rates are shown for three products for ~80 min near closest approach to MU_{69} (indicated by the vertical black line). Data were acquired in 1-s bins but averaged over 2-min intervals to improve the signal-to-noise ratio. (F) Suprathermal particles at >2 keV $nucleon^{-1}$ (dominated by interstellar pickup He^+); (G) energetic protons (30 keV to 1 MeV); (H) galactic cosmic rays (mostly >100 MeV protons); (I) the angle between PEPSSI aperture and the Sun. Changes in instrument orientation account for all the observed count rate variability; all particle rates shown are typical for the undisturbed interplanetary medium, with an increased photon background when the Sun is in the PEPSSI field of view (FOV).

both. This suggests that contact binaries may be rare in CCKBO systems with orbiting satellites. Another possibility, however, is that the lobes Ultima and Thule impacted one another multiple times, shedding mass along with angular momentum before making final contact. But the alignment of the principal axes of MU_{69} s two lobes tends to disfavor this hypothesis. In contrast, tidal locking could quite plausibly have produced the principal axis alignment we observe, once the co-orbiting bodies were close enough and spin-orbit coupling was most effective (*76*). Gas drag could also have played a role in fostering the observed coplanar alignment of the Ultima and Thule lobes (Fig. 2). Post-merger impacts may have also somewhat affected the observed, final angular momentum state.

Methods

Shape model fitting process

Because the pole and rotation rate of MU_{69} were not known before the New Horizons flyby, it was necessary to simultaneously fit the shape and pole of the object. The data available to accomplish this were the resolved images of MU_{69} that were obtained from a few days prior to closest approach up to closest approach itself. The problem was broken into parameters for pole, rotation rate, mean surface albedo, and a parametrically defined shape. Each of the two lobes of the KBO was defined with its own parametric model; the separation between the lobes was made an additional free parameter. The "octantoid" formalism was used for the lobes (*30*), which is similar to spherical harmonics but is precisely an ellipsoid at the lowest order. Starting by assuming that both lobes are ellipsoids, increasing complexity and spatial resolution were then added to the shape model by increasing the harmonic orders of the octantoids. Images were converted to radiometrically calibrated *I F* space to minimize the work the fitting program would have to do.

To test this parameter set against the data, synthetic versions of the resolved images were generated as follows. First, the parametric shape was rastered onto a 3D mesh for each lobe, and the surface normals for each polygon in the mesh were calculated. Next, the geometry for the image was calculated, using the navigation SPICE kernels (*77*) for distance to MU_{69} and the World Coordinate System (WCS) for pixel scale and image rotation. The mesh was then rendered in OpenGL using the derived geometry. The renders were performed twice, once to provide a depth buffer and a second time that used the depth buffer to allow self-shadowing on the object. The second rendering also calculated the brightness for each pixel of the image in *I F* space, using the Hapke photometric model described in the text. Performing the rendering in OpenGL allowed the work to use GPUs to speed up the shape-fitting process. The rendered images from each New Horizons camera were then convolved with the point-spread function of that camera. This smeared out the rendered images to the same angular resolution as the real images, allowing direct comparison of the images on a pixel-by-pixel basis, even in the early images in which MU_{69} was only a few pixels long. Finally, the sum of the square of the difference of each real image was compared to its simulated version; a sum of all of those differences provides an estimate of the χ^2 for any derived parameter set.

With the problem now reduced to a parameter set and a χ^2 function, standard function-minimization techniques were used to find the optimal shape and pole. As noted above, this started with simple ellipsoidal shapes for each lobe, which were used to find initial solutions for the pole, rotation, and obliquity. Next, the complexity of the model shapes was gradually increased as new images were incorporated. The number of images fitted and the complexity of the model both increased the time to calculate χ^2 for any parameter set, and thus increased the time required for the optimization process. This in turn limited the spatial resolution of the shape model.

LEIS data processing

The IR spectral imaging spectroscopy capability on New Horizons is provided by the LEISA instrument (*78*). LEISA s focal plane consists of a 256 × 256 HgCdTe detector array with a linear variable filter affixed to it such that each row of the array is sensitive to a different IR wavelength between 1.2 and 2.5 μm. Its average spectral resolving power (λ/ λ) is close to 240. LEISA is operated by sweeping its field of view across the target scene while images are recorded at a frame rate of approximately 1 frame per pixel moved, so that each part of the scene is recorded in each of LEISA s wavelengths. The highest spatial resolution LEISA scan of MU_{69} was designated CA04_LE. This scan can also be identified by its unique Mission Elapsed Time (MET) number, 0408624118; it was obtained about 4:58 UT on 1 January, approximately 35 min before closest approach, and from a mean spacecraft range of 31,000 km. LEISA s pixel scale maps to 1.9 km on MU_{69} at that range. Without knowledge of the exact shape or spin state of MU_{69}, we could not map the signal recorded in each of LEISA s spectral pixels to their exact locations on the surface of the body. Instead, we mapped them to a tangent plane oriented perpendicular to the spacecraft-MU_{69} line of sight, located at the distance of MU_{69}. Attitude data reported by the spacecraft were used to account for the motion of the target through the LEISA field of view. This motion was complex because spacecraft pointing was controlled by frequent thruster firings to maintain pointing within a specified amount. Over the course of the scan, the spacecraft also closed range with the target, from approximately 33,000 to 29,000 km. This changing geometry resulted in a wavelength-dependent scale in the spectral image cube. To correct for this effect in extracting the spectrum shown in Fig. 5D, the region of interest for spectral extraction was constructed using the same wavelength-dependent scale. The diminished solar flux at 43 AU, combined with the low albedo of MU_{69}, produces a signal level similar to the noise in a single LEISA pixel, so multiple pixels had to be averaged together to produce the spectrum in Fig. 5D. The scatter of the points gives an indication of the noise in the resulting average spectrum. Spectral models of granular combinations of H_2O and CH_3OH ices with tholins are able to reproduce the overall albedo and features in the LEISA spectrum, except for the unidentified band at 1.8 μm.

Thermal models

Incident sunlight varies across MU_{69} s surface over its 293-year orbit around the Sun and also its 15.92-hour rotation about its spin axis, causing time-variable temperatures. The local radiative balance is also affected by topography, especially in the neck region, where greater shadowing reduces incident sunlight but also reduces the solid angle of dark sky into which thermal emission can be radiated. Heat propagating inward or outward moderates insolation-driven surface temperature variations, with thermal inertia Γ (the square root of the product of heat capacity *c*, density ρ, and conductivity of the material *k*, with units of J m^{-2} $s^{-1/2}$ K^{-1}) controlling the degree of moderation. The thermal waves penetrate to a characteristic skin depth, $d_{skin} = (2k/\omega\rho c)^{1/2}$, where ω is the angular frequency of the temperature forcing. Conductivity is the least certain of these parameters, being sensitively dependent on the material texture and temperature. It is generally low for cold, granular materials in vacuum, and the expectation for MU_{69} is for very loosely consolidated material. This follows from the low expected bulk density of MU_{69}, as well as from thermal observations of other KBOs. Herschel and Spitzer space telescope observations have shown a mean diurnal thermal inertia for Centaurs and KBOs of ~2.5 J m^{-2} $s^{-1/2}$ K^{-1} (*52*). Assuming a bulk density of 500 kg m^{-3} and a heat capacity of 350 J kg^{-1} K^{-1} of H_2O-ice at 40 K (*79*), a Γ of 2.5 J m^{-2} $s^{-1/2}$ K^{-1} implies a very low conductivity of approximately 3.6×10^{-5} J m^{-1} s^{-1} K^{-1}. If instead we follow (*80*, *81*) and assume that ice Ih is the dominant constituent, such a low conductivity would require a porosity of ~65 , not unreasonable for a bulk density of 500 kg m^{-3}.

Low thermal inertia and low conductivity imply that surface temperatures on MU_{69} are close to instantaneous equilibrium between absorbed insolation and thermal emission. The low conductivity implies that the thermal waves driven by diurnal and seasonal insolation variations affect only the very outermost layers, with d_{skin} = 0.001 m and ~1 m, respectively. The seasonal skin depth could be somewhat greater if conductivity increases with depth below the surface. MU_{69} could have an even lower thermal inertia than the much larger objects in the Herschel and Spitzer sample, given that its lower mass and sparseness of impact craters imply less collisional compaction over time and that its smaller size limits the possibility of early heating by short-lived radionuclides that might have led to sintering and thus higher thermal conductivity in larger objects.

REFERENCES AND NOTES

1. J. K. Davies, J. McFarland, M. E. Bailey, B. G. Marsden, W.-H. Ip, in *The Solar System Beyond Neptune*, M. A. Barucci, H. Boehnhardt, D. P. Cruikshank, A. Morbidelli, Eds. Univ. of Arizona Press, 2008), pp. 11–23.
2. National Research Council, *New Frontiers in the Solar System: An Integrated Exploration Strategy* National Academies Press, 2003). doi: 10.17226/10432
3. C. T. Russell, Ed., *New Horizons: Reconnaissance of the Pluto Charon System and the Kuiper Belt* Springer, 2008).
4. S. A. Stern *et al*., The Pluto system: Initial results from its exploration by New Horizons. *Science* **350**, aad1815 2015). doi: 10.1126/science.aad1815; pmid: 26472913
5. S. A. Stern, W. M. Grundy, W. B. McKinnon, H. A. Weaver, L. A. Young, The Pluto system after New Horizons. *Annu. Rev. Astron. Astrophys.* **56**, 357–392 2018). doi: 10.1146/annurev-astro-081817-051935
6. S. A. Stern, H. A. Weaver, J. R. Spencer, H. A. Elliott, The New Horizons Kuiper Belt Extended Mission. *Space Sci. Rev.* **214**, 77 2018). doi: 10.1007/s11214-018-0507-4
7. M. W. Buie *et al*., "Pre-encounter update on 486958) 2014MU_{69} and occultation results from 2017 and 2018." Paper presented at the 50th AAS/Division of Planetary Sciences Meeting, 21–26 October 2018, Knoxville, TN, abstract 509.06; http://adsabs.harvard.edu/abs/2018DPS....5050906B.
8. S. B. Porter *et al*., High-precision orbit fitting and uncertainty analysis of 486958 2014 MU_{69}). *Astron. J.* **156**, 20 2018). doi: 10.3847/1538-3881/aac2e1
9. S. D. Benecchi, S. Sheppard, Light curves of 32 large Transneptunian objects. *Astron. J.* **145**, 124–143 2013). doi: 10.1088/0004-6256/145/5/124
10. S. D. Benecchi *et al*., The HST lightcurve of 486958) 2014 MU_{69}. *Icarus* 10.1016/j.icarus.2019.01.023 2019). doi: 10.1016/j.icarus.2019.01.023
11. K. Tsiganis, R. Gomes, A. Morbidelli, H. F. Levison, Origin of the orbital architecture of the giant planets of the Solar System. *Nature* **435**, 459–461 2005). doi: 10.1038/nature03539; pmid: 15917800
12. D. Nesvorný, Dynamical evolution of the early Solar System. *Annu. Rev. Astron. Astrophys.* **56**, 137–174 2018). doi: 10.1146/annurev-astro-081817-052028
13. S. C. Tegler, W. Romanishin, Two distinct populations of Kuiper-belt objects. *Nature* **392**, 49–51 1998). doi: 10.1038/32108; pmid: 9510246
14. W. C. Fraser, M. E. Brown, M. E. Schwamb, The luminosity function of the hot and cold Kuiper belt populations. *Icarus* **210**, 944–955 2010). doi: 10.1016/j.icarus.2010.08.001
15. E. Vilenius *et al*., "TNOs are Cool": A survey of the trans-Neptunian region X. Analysis of classical Kuiper belt objects from Herschel and Spitzer observations. *Astron. Astrophys.* **564**, A35 2014). doi: 10.1051/0004-6361/201322416
16. K. S. Noll, W. M. Grundy, E. I. Chiang, J.-L. Margot, S. D. Kern, in *The Solar System Beyond Neptune*, M. A. Barucci, H. Boehnhardt, D. P. Cruikshank, A. Morbidelli, Eds. Univ. of Arizona Press, 2008), pp. 345–364.
17. D. T. Britt *et al*., The morphology and surface processes of Comet 19/P Borrelly. *Icarus* **167**, 45–53 2004). doi: 10.1016/j.icarus.2003.09.004
18. P. C. Thomas *et al*., Shape, density, and geology of the nucleus of Comet 103P/Hartley 2. *Icarus* **222**, 550–558 2013). doi: 10.1016/j.icarus.2012.05.034
19. L. Jorda *et al*., The global shape, density and rotation of Comet 67P/Churyumov-Gerasimenko from pre-perihelion Rosetta/OSIRIS observations. *Icarus* **277**, 257–278 2016). doi: 10.1016/j.icarus.2016.05.002
20. M. Massironi *et al*., Two independent and primitive envelopes of the bilobate nucleus of comet 67P. *Nature* **526**, 402–405 2015). doi: 10.1038/nature15511; pmid: 26416730
21. B. J. R. Davidsson *et al*., The primordial nucleus of comet 67P/Churyumov-Gerasimenko. *Astron. Astrophys.* **592**, A63–A93 2016). doi: 10.1051/0004-6361/201526968
22. M. Jutzi, W. Benz, Formation of bi-lobed shapes by sub-catastrophic collisions: A late origin of comet 67P s structure. *Astron. Astrophys.* **597**, A62–A72 2017). doi: 10.1051/0004-6361/201628964
23. S. Greenstreet, B. Gladman, W. McKinnon, J. J. Kavelaars, K. Singer, Crater density predictions for New Horizons flyby target 2014 MU_{69}. *Astrophys. J.* **872**, L5 2019). doi: 10.3847/2041-8213/ab01db
24. D. Nesvorný, A. N. Youdin, D. C. Richardson, Formation of Kuiper Belt binaries by gravitational collapse. *Astron. J.* **140**, 785–793 2010). doi: 10.1088/0004-6256/140/3/785
25. W. C. Fraser *et al*., All planetesimals born near the Kuiper belt formed as binaries. *Nat. Astron.* **1**, 0088 2017). doi: 10.1038/s41550-017-0088
26. D. Perna *et al*., Rotations and densities of trans-Neptunian objects. *Astron. Astrophys.* **508**, 451–455 2009). doi: 10.1051/0004-6361/200911970
27. A. Thirouin *et al*., Short-term variability of a sample of 29 trans-Neptunian objects and Centaurs. *Astron. Astrophys.* **522**, A93 2010). doi: 10.1051/0004-6361/200912340
28. D. P. Rubincam, Radiative spin-up and spin-down of small asteroids. *Icarus* **148**, 2–11 2000). doi: 10.1006/icar.2000.6485
29. D. Vokrouhlicky, W. F. Bottke, S. R. Chesley, D. J. Scheeres, T. S. Statler, in *Asteroids IV*, P. Michel, F. E. DeMeo, W. F. Bottke, Eds. Univ. of Arizona Press, 2015), pp. 509–532.
30. M. Kaasalainen, M. Viikinkoski, Shape reconstruction of irregular bodies with multiple complementary data sources. *Astron. Astrophys.* **543**, A97 2012). doi: 10.1051/0004-6361/201219267
31. S. Charnoz, A. Brahic, P. C. Thomas, C. C. Porco, The equatorial ridges of Pan and Atlas: Terminal accretionary ornaments? *Science* **318**, 1622–1624 2007). doi: 10.1126/science.1148631; pmid: 18063797
32. M. Jutzi, E. Asphaug, The shape and structure of cometary nuclei as a result of low-velocity accretion. *Science* **348**, 1355–1358 2015). doi: 10.1126/science.aaa4747; pmid: 26022415
33. M. Pätzold *et al*., A homogeneous nucleus for comet 67P/Churyumov-Gerasimenko from its gravity field. *Nature* **530**, 63–65 2016). doi: 10.1038/nature16535; pmid: 26842054
34. P. M. Schenk, R. R. Wilson, A. G. Davies, Shield volcano topography and the rheology of lava flows on Io. *Icarus* **169**, 98–110 2004). doi: 10.1016/j.icarus.2004.01.015
35. R. A. Beyer, O. Alexandrov, S. McMichael, The Ames Stereo Pipeline: NASA s Open Source Software for Deriving and Processing Terrain Data. *Earth Space Sci.* **5**, 537–548 2018). doi: 10.1029/2018EA000409; pmid: 26022415
36. A. L. Souchon *et al*., An experimental study of Hapke s modeling of natural granular surface samples. *Icarus* **215**, 313–331 2011). doi: 10.1016/j.icarus.2011.06.023
37. A. F. McGuire, B. W. Hapke, An experimental study of light scattering by large, irregular particles. *Icarus* **113**, 134–155 1995). doi: 10.1006/icar.1995.1012
38. P. Lacerda *et al*., The albedo-color diversity of transneptunian objects. *Astrophys. J.* **793**, L2 2014). doi: 10.1088/2041-8205/793/1/L2
39. A. Doressoundiram, H. Boehnhardt, S. C. Tegler, C. Trujillo, in *The Solar System Beyond Neptune*, M. A. Barucci, H. Boehnhardt, D. Cruikshank, A. Morbidelli, Eds. Univ. of Arizona Press, 2008), pp. 91–104.
40. O. R. Hainaut, H. Boehnhardt, S. Protopapa, Colors of minor bodies in the outer Solar System II. A statistical analysis revisited. *Astron. Astrophys.* **546**, A115 2012). doi: 10.1051/0004-6361/201219566
41. R. E. Pike *et al*., Col-OSSOS: z-band photometry reveals three distinct TNO surface types. *Astron. J.* **154**, 101 2017). doi: 10.3847/1538-3881/aa83b1
42. S. D. Benecchi *et al*., The correlated colors of transneptunian binaries. *Icarus* **200**, 292–303 2009). doi: 10.1016/j.icarus.2008.10.025
43. D. P. Cruikshank, H. Imanaka, C. M. Dalle Ore, Tholins as coloring agents on outer Solar System bodies. *Adv. Space Res.* **36**, 178–183 2005). doi: 10.1016/j.asr.2005.07.026
44. R. Brunetto, M. A. Barucci, E. Dotto, G. Strazzulla, Ion irradiation of frozen methanol, methane, and benzene: Linking to the colors of Centaurs and trans-Neptunian objects. *Astrophys. J.* **644**, 646–650 2006). doi: 10.1086/503359
45. M. A. Barucci, F. Merlin, E. Dotto, A. Doressoundiram, C. de Bergh, TNO surface ices: Observations of the TNO 55638 2002 VE_{95}) and analysis of the population s spectral properties. *Astron. Astrophys.* **455**, 725–730 2006). doi: 10.1051/0004-6361:20064951
46. D. P. Cruikshank *et al*., The composition of centaur 5145 Pholus. *Icarus* **135**, 389–407 1998). doi: 10.1006/icar.1998.5997
47. F. Merlin, E. Quirico, M. A. Barucci, C. de Bergh, Methanol ice on the surface of minor bodies in the Solar System. *Astron. Astrophys.* **544**, A20 2012). doi: 10.1051/0004-6361/201219181
48. W. M. Grundy *et al*., Pluto s haze as a surface material. *Icarus* **314**, 232–245 2018). doi: 10.1016/j.icarus.2018.05.019
49. R. N. Clark, P. G. Lucey, Spectral properties of ice-particulate mixtures and implications for remote sensing: 1. Intimate mixtures. *J. Geophys. Res.* **89**, 6341–6348 1984). doi: 10.1029/JB089iB07p06341
50. D. O. Muhleman, G. L. Berge, D. Rudy, A. E. Niell, Precise VLA positions and flux-density measurements of the Jupiter system. *Astron. J.* **92**, 1428–1435 1986). doi: 10.1086/114279
51. S. J. Ostro *et al*., Cassini RADAR observations of Enceladus, Tethys, Dione, Rhea, Iapetus, Hyperion, and Phoebe. *Icarus* **183**, 479–490 2006). doi: 10.1016/j.icarus.2006.02.019
52. E. Lellouch *et al*., "TNOs are Cool": A survey of the trans-Neptunian region IX. Thermal properties of Kuiper belt objects and Centaurs from combined Herschel and Spitzer observations. *Astron. Astrophys.* **557**, A60 2013). doi: 10.1051/0004-6361/201322047
53. F. Nimmo *et al*., Mean radius and shape of Pluto and Charon from New Horizons images. *Icarus* **287**, 12–29 2017). doi: 10.1016/j.icarus.2016.06.027
54. J. M. Moore, M. T. Mellon, A. P. Zent, Mass Wasting and Ground Collapse in Terrains of Volatile-Rich Deposits as a Solar System-Wide Geological Process: The Pre-Galileo View. *Icarus* **122**, 63–78 1996). doi: 10.1006/icar.1996.0109
55. J. M. Moore *et al*., Mass Movement and Landform Degradation on the Icy Galilean Satellites: Results of the Galileo Nominal Mission. *Icarus* **140**, 294–312 1999). doi: 10.1006/icar.1999.6132
56. J. M. Moore *et al*., Great expectations: Plans and predictions for New Horizons encounter with Kuiper Belt Object 2014 MU_{69} "Ultima Thule"). *Geophys. Res. Lett.* **45**, 8111 2018).
57. M. J. S. Belton *et al*., The internal structure of Jupiter family cometary nuclei from Deep Impact observations: The "talps" or "layered pile" model. *Icarus* **187**, 332–344 2007). doi: 10.1016/j.icarus.2006.09.005
58. F. Braga-Ribas *et al*., A ring system detected around the Centaur 10199) Chariklo. *Nature* **508**, 72–75 2014). doi: 10.1038/nature13155; pmid: 24670644
59. J. L. Ortiz *et al*., The size, shape, density and ring of the dwarf planet Haumea from a stellar occultation. *Nature* **550**, 219–223 2017). doi: 10.1038/nature24051; pmid: 29022593
60. D. P. Hamilton, Deadly Sunflower Orbits. *AAS/Division of Dynamical Astronomy Meeting*, **9**, 401.02 2018); http://adsabs.harvard.edu/abs/2018DDA....4940102H.
61. L. W. Esposito, Planetary rings. *Rep. Prog. Phys.* **65**, 1741–1760 2002). doi: 10.1088/0034-4885/65/12/201
62. H. B. Throop *et al*., The jovian rings: New results derived from Cassini, Galileo, Voyager, and Earth-based observations. *Icarus* **172**, 59–77 2004). doi: 10.1016/j.icarus.2003.12.020
63. M. E. Brown, E. L. Schaller, W. C. Fraser, A hypothesis for the color diversity of the Kuiper Belt. *Astrophys. J.* **739**, L60 2011). doi: 10.1088/2041-8205/739/2/L60
64. C. M. Dalle Ore *et al*., The composition of "ultra-red" TNOs and centaurs. *Icarus* **252**, 311–326 2015). doi: 10.1016/j.icarus.2015.01.014
65. G. R. Gladstone, W. R. Pryor, S. A. Stern, Lyα@Pluto. *Icarus* **246**, 279 2015). doi: 10.1016/j.icarus.2014.04.016
66. G. R. Gladstone *et al*., The Lyman-α sky background as observed by New Horizons. *Geophys. Res. Lett.* **45**, 8022 2018).
67. M. S. Westley, R. A. Baragiola, R. E. Johnson, G. A. Baratta, Ultraviolet photodesorption from water ice. *Planet. Space Sci.* **43**, 1311–1315 1995). doi: 10.1016/0032-0633 95)00088-M
68. K. I. Öberg, H. Linnartz, R. Visser, E. F. van Dishoeck, Photodesorption of ices: II. H_2O and D_2O. *Astrophys. J.* **693**, 1209–1218 2009). doi: 10.1088/0004-637X/693/2/1209
69. C. Arasa, J. Koning, G.-J. Kroes, C. Walsh, E. F. van Dishoeck, Photodesorption of H_2O, HDO, and D_2O ice and its impact on fractionation. *Astron. Astrophys.* **575**, A121 2015). doi: 10.1051/0004-6361/201322695
70. E. A. Muntean *et al*., A laboratory study of water ice erosion by low-energy ions. *Mon. Not. R. Astron. Soc.* **462**, 3361–3367 2016). doi: 10.1093/mnras/stw1855
71. W. B. McKinnon *et al*., "A pristine 'contact binary in the Kuiper belt: Implications from the New Horizons encounter with 2014 MU_{69} 'Ultima Thule)." Paper presented at the 50th Lunar and Planetary Science Conference, The Woodlands, TX, 18–22 March 2019, abstract 2767; www.hou.usra.edu/meetings/lpsc2019/pdf/2767.pdf.
72. O. M. Umurhan *et al*., "Ultima Thule: Possible Gravitational Collapse Scenarios for its Origin." Paper presented at the 50th Lunar and Planetary Science Conference, The Woodlands, TX, 18–22 March 2019, abstract 2809; www.hou.usra.edu/meetings/lpsc2019/pdf/2809.pdf.
73. J. N. Cuzzi, R. C. Hogan, W. F. Bottke, Towards initial mass functions for asteroids and Kuiper Belt objects. *Icarus* **208**, 518–538 2010). doi: 10.1016/j.icarus.2010.03.005
74. P. Goldreich, Y. Lithwick, R. Sari, Formation of Kuiper-belt binaries by dynamical friction and three-body encounters.

Nature **420**, 643–646 2002). doi: 10.1038/nature01227; pmid: 12478286
75. H. E. Schlichting, R. Sari, The ratio of retrograde to prograde orbits: A test for Kuiper belt binary formation theories. *Astrophys. J.* **686**, 741–747 2009). doi: 10.1086/591073
76. C. D. Murray, S. F. Dermott, *Solar System Dynamics* Cambridge Univ. Press, 1999).
77. https://naif.jpl.nasa.gov/naif/spiceconcept.html.
78. D. C. Reuter *et al*., Ralph: A visible/infrared imager for the New Horizons Pluto/Kuiper belt mission. *Space Sci. Rev.* **140**, 129–154 2008). doi: 10.1007/s11214-008-9375-7
79. J. R. Spencer, J. M. Moore, The influence of thermal inertia on temperatures and frost stability on Triton. *Icarus* **99**, 261–272 1992). doi: 10.1016/0019-1035 92)90145-W
80. J. C. Castillo-Rogez *et al*., Iapetus geophysics: Rotation rate, shape, and equatorial ridge. *Icarus* **190**, 179–202 2007). doi: 10.1016/j.icarus.2007.02.018
81. J. C. Castillo-Rogez *et al*., Geophysical evolution of Saturn s satellite Phoebe, a large planetesimal in the outer Solar System. *Icarus* **219**, 86–109 2012). doi: 10.1016/j.icarus.2012.02.002
82. B. Hapke, *Theory of Reflectance and Emittance Spectroscopy* Cambridge Univ. Press, ed. 2, 2012).
83. J.-Y. Li *et al*., Photometric properties of the nucleus of Comet 103P/Hartley 2. *Icarus* **222**, 559–570 2013). doi: 10.1016/j.icarus.2012.11.001
84. M. F. A Hearn *et al*., EPOXI at comet Hartley 2. *Science* **332**, 1396–1400 2011). doi: 10.1126/science.1204054; pmid: 21680835

ACKNOWLEDGMENTS

We thank all ~2500 present and past New Horizons team members, NASA and its Deep Space Network, KinetX Aerospace Corporation, the Caltech Jet Propulsion Laboratory, and the European Space Agency Gaia and NASA HST space missions for their contributions to making the flyby of MU_{69} successful; our NASA Headquarters Program Scientist, C. Niebur; and J. Anderson of the Space Telescope Science Institute. We also thank NASA Administrator J. Bridenstine for his key support during the December 2018 to January 2019 partial U.S. government shutdown; SwRI President A. Hamilton and Johns Hopkins Applied Physics Laboratory Director R. Semmel for many years of valuable project support; and three anonymous referees for their helpful contributions to this paper. We acknowledge the contributions of our late team members Thomas Coughlin, Robert Farquhar, William Gibson, Lisa Hardaway, and David C. Slater. **Funding:** Supported by NASA s New Horizons project via contracts NASW-02008 and NAS5-97271/TaskOrder30. Also supported by the National Research Council of Canada J.J.K.). **Author contributions:** S.A.S., J.R.S., J.M.M., O.L.W., W.B.M., W.M.G., G.R.G., and H.A.E. were responsible for drafting this manuscript. S.A.S. is the principal investigator of the New Horizons mission. All other authors participated in mission planning, mission operations, mission engineering, mission management, mission public affairs, or science data reduction or analysis, and/or provided inputs and critique to this manuscript. **Competing interests:** We declare no competing interests. **Data and materials availability:** All images, spacecraft data, and the shape model used in this paper are available at http://dx.doi.org/10.6084/m9.figshare.7940630. Additional fully calibrated New Horizons MU_{69} data and higher-order data products will be released by the NASA Planetary Data System at https://pds-smallbodies.astro.umd.edu/data_sb/missions/newhorizons/index.shtml in a series of stages in 2020 and 2021, owing to the time required to fully downlink and calibrate the dataset.

20 February 2019; accepted 16 April 2019
10.1126/science.aaw9771

Science

Initial results from the New Horizons exploration of 2014 MU_{69}, a small Kuiper Belt object

S. A. Stern, H. A. Weaver, J. R. Spencer, C. B. Olkin, G. R. Gladstone, W. M. Grundy, J. M. Moore, D. P. Cruikshank, H. A. Elliott, W. B. McKinnon, J. Wm. Parker, A. J. Verbiscer, L. A. Young, D. A. Aguilar, J. M. Albers, T. Andert, J. P. Andrews, F. Bagenal, M. E. Banks, B. A. Bauer, J. A. Bauman, K. E. Bechtold, C. B. Beddingfield, N. Behrooz, K. B. Beisser, S. D. Benecchi, E. Bernardoni, R. A. Beyer, S. Bhaskaran, C. J. Bierson, R. P. Binzel, E. M. Birath, M. K. Bird, D. R. Boone, A. F. Bowman, V. J. Bray, D. T. Britt, L. E. Brown, M. R. Buckley, M. W. Buie, B. J. Buratti, L. M. Burke, S. S. Bushman, B. Carcich, A. L. Chaikin, C. L. Chavez, A. F. Cheng, E. J. Colwell, S. J. Conard, M. P. Conner, C. A. Conrad, J. C. Cook, S. B. Cooper, O. S. Custodio, C. M. Dalle Ore, C. C. Deboy, P. Dharmavaram, R. D. Dhingra, G. F. Dunn, A. M. Earle, A. F. Egan, J. Eisig, M. R. El-Maarry, C. Engelbrecht, B. L. Enke, C. J. Ercol, E. D. Fattig, C. L. Ferrell, T. J. Finley, J. Firer, J. Fischetti, W. M. Folkner, M. N. Fosbury, G. H. Fountain, J. M. Freeze, L. Gabasova, L. S. Glaze, J. L. Green, G. A. Griffith, Y. Guo, M. Hahn, D. W. Hals, D. P. Hamilton, S. A. Hamilton, J. J. Hanley, A. Harch, K. A. Harmon, H. M. Hart, J. Hayes, C. B. Hersman, M. E. Hill, T. A. Hill, J. D. Hofgartner, M. E. Holdridge, M. Horányi, A. Hosadurga, A. D. Howard, C. J. A. Howett, S. E. Jaskulek, D. E. Jennings, J. R. Jensen, M. R. Jones, H. K. Kang, D. J. Katz, D. E. Kaufmann, J. J. Kavelaars, J. T. Keane, G. P. Keleher, M. Kinczyk, M. C. Kochte, P. Kollmann, S. M. Krimigis, G. L. Kruizinga, D. Y. Kusnierkiewicz, M. S. Lahr, T. R. Lauer, G. B. Lawrence, J. E. Lee, E. J. Lessac-Chenen, I. R. Linscott, C. M. Lisse, A. W. Lunsford, D. M. Mages, V. A. Mallder, N. P. Martin, B. H. May, D. J. McComas, R. L. McNutt Jr., D. S. Mehoke, T. S. Mehoke, D. S. Nelson, H. D. Nguyen, J. I. Núñez, A. C. Ocampo, W. M. Owen, G. K. Oxton, A. H. Parker, M. Pätzold, J. Y. Pelgrift, F. J. Pelletier, J. P. Pineau, M. R. Piquette, S. B. Porter, S. Protopapa, E. Quirico, J. A. Redfern, A. L. Regiec, H. J. Reitsema, D. C. Reuter, D. C. Richardson, J. E. Riedel, M. A. Ritterbush, S. J. Robbins, D. J. Rodgers, G. D. Rogers, D. M. Rose, P. E. Rosendall, K. D. Runyon, M. G. Ryschkewitsch, M. M. Saina, M. J. Salinas, P. M. Schenk, J. R. Scherrer, W. R. Schlei, B. Schmitt, D. J. Schultz, D. C. Schurr, F. Scipioni, R. L. Sepan, R. G. Shelton, M. R. Showalter, M. Simon, K. N. Singer, E. W. Stahlheber, D. R. Stanbridge, J. A. Stansberry, A. J. Steffl, D. F. Strobel, M. M. Stothoff, T. Stryk, J. R. Stuart, M. E. Summers, M. B. Tapley, A. Taylor, H. W. Taylor, R. M. Tedford, H. B. Throop, L. S. Turner, O. M. Umurhan, J. Van Eck, D. Velez, M. H. Versteeg, M. A. Vincent, R. W. Webbert, S. E. Weidner, G. E. Weigle II, J. R. Wendel, O. L. White, K. E. Whittenburg, B. G. Williams, K. E. Williams, S. P. Williams, H. L. Winters, A. M. Zangari and T. H. Zurbuchen

Science **364** (6441), eaaw9771.
DOI: 10.1126/science.aaw9771

New Horizons flies past MU_{69}

After flying past Pluto in 2015, the New Horizons spacecraft shifted course to encounter (486958) 2014 MU_{69}, a much smaller body about 30 kilometers in diameter. MU_{69} is part of the Kuiper Belt, a collection of small icy bodies orbiting in the outer Solar System. Stern *et al.* present the initial results from the New Horizons flyby of MU_{69} on 1 January 2019. MU_{69} consists of two lobes that appear to have merged at low speed, producing a contact binary. This type of Kuiper Belt object is mostly undisturbed since the formation of the Solar System and so will preserve clues about that process.

Science, this issue p. eaaw9771

Science (print ISSN 0036-8075; online ISSN 1095-9203) is published by the American Association for the Advancement of Science, 1200 New York Avenue NW, Washington, DC 20005. The title *Science* is a registered trademark of AAAS.

Science (print ISSN 0036-8075; online ISSN 1095-9203) is published by the American Association for the Advancement of Science, 1200 New York Avenue NW, Washington, DC 20005. The title *Science* is a registered trademark of AAAS.